An improved method of Newmark analysis for mapping hazards of coseismic landslides

Mingdong Zang[1,2,3], Shengwen Qi[1,2,3], Yu Zou[1,2,3], Zhuping Sheng[4], Blanca S. Zamora[4]

[1]Key Laboratory of Shale Gas and Geoengineering, Institute of Geology and Geophysics, Chinese Academy of Sciences, Beijing 100029, China

[2]Institutions of Earth Science, Chinese Academy of Sciences, Beijing 100029, China

[3]University of Chinese Academy of Sciences, Beijing 100029, China

[4]Texas A&M AgriLife Research Center at El Paso, El Paso, Texas 79927, USA

Correspondence to: Shengwen Qi (qishengwen@mail.iggcas.ac.cn)

Abstract. Coseismic landslides can destroy buildings, dislocate roads, sever pipelines, and cause heavy casualties. It is thus important but challenging to accurately map the hazards posed by coseismic landslides. Newmark's method is widely applied to assess the permanent displacement along a potential slide surface and model the coseismic response of slopes. This paper proposes an improved Newmark analysis for mapping the hazards of coseismic landslides by considering the roughness and effect of size of the potential slide surfaces. This method is verified by data from a case study on the 2014 M_w 6.1 (the United States Geological Survey) Ludian earthquake in Yunnan Province of China. Permanent displacements due to the earthquake ranged from 0 to 122 cm. The predicted displacements were compared with a comprehensive inventory of landslides triggered by the Ludian earthquake to map the spatial variation in the hazards of coseismic landslides using the certainty factor model. The confidence levels of coseismic landslides indicated by the certainty factors ranged from -1 to 0.95. A hazard map of the coseismic landslide was generated based on the spatial distribution of values of the certainty factor. A regression curve relating the predicted displacement and the certainty factor was drawn, and can be applied to predict the hazards of coseismic landslides for any seismic scenario of interest. The area under the curve was used to compare the improved and the conventional Newmark analyses, and revealed the improved performance of the former. This mapping procedure can be used to predict the hazards posed by coseismic landslides, and provide guidelines for decisions regarding the development of infrastructure and post-earthquake reconstruction.

Keywords: Coseismic landslide; Newmark's method; Barton model; Certainty factor; Hazard mapping

1 Introduction

Earthquakes are recognized as one of the major causes of landslides (Keefer, 1984). Hazards caused by coseismic landslides have drawn increasing attention in recent years (e.g., Jibson et al., 1998, 2000; Khazai and Sitar, 2004; Qi et al., 2010, 2011, 2012; Chen et al., 2012; Xu et al., 2013; Yuan et al., 2014). The damage caused by seismically triggered landslides is sometimes more severe than the direct damage caused by the earthquake (Keefer, 1984). Estimating where a specific shaking is likely to induce a slope failure plays an important role in the regional assessment of coseismic landslides.

Pseudostatic analysis formalized by Terzaghi (1950), and finite-element modeling applied by Clough and Chopra (1966) have been employed to assess the seismic stability of slopes in early efforts (Jibson, 2011). Newmark (1965) first introduced a relatively simple and practical method, which is still commonly used nowadays, to estimate the coseismic permanent displacements of slopes (Jibson, 2011). Studies have shown that Newmark's method yields reasonable and practical results when modeling the dynamic performance of natural slopes (Wilson and Keefer, 1983; Wieczorek et al., 1985; Jibson et al., 1998, 2000; Pradel et al., 2005). Rathje and Antonakos (2011) recently presented a unified framework for predicting coseismic permanent sliding displacement based on Newmark's method. Chen et al. (2018) used Newmark's method to calculate the minimum accelerations required for coseismic landslides in the region affected by the 2014 Ludian earthquake. Chen et al. (2019) subsequently developed an easy-operation mapping method to assess hazards posed by coseismic landslides in the zone struck by the 2014 Ludian earthquake using Newmark's method.

Such applications generally start from an analysis of the dynamic stability of slopes, which is quantified as the critical acceleration. Barton model (Barton, 1973) has been widely used in rock mechanics and

56 engineering to predict the shear strength of rock joints, which plays a crucial role in the calculation of

57 critical acceleration. However, researchers have not adequately attended to the shear strength of rock

58 joints during the assessment of coseismic landslides. To better estimate the dynamic stability of slopes, in

59 this paper, we introduce the Barton model (Barton, 1973) to Newmark analysis to develop an improved

60 modeling method for mapping the hazards posed by coseismic landslides using data from the 2014 Ludian

61 earthquake in Yunnan Province in southwestern China. As predictions of coseismic landslides are not

62 based on exact results, i.e., the computed permanent displacements, but are also mingled with

63 unformalized expertise, i.e., the interpreted landslides, we present a model of inexact reasoning, i.e., the

64 certainty factor model (CFM), that defies analysis, as an application of sets of inference rules that are

65 expressed in predicate logic (Shortliffe and Buchanan, 1975), to produce a map of the hazards posed by

66 coseismic landslides.

67 This paper briefly introduces the characteristics and spatial distribution of landslides triggered at the

68 chosen site, describes the method of modeling used for the analysis of the stability of seismic slopes,

69 presents the mapping procedure of the confidence level of seismic slope failure, and finally discusses the

70 results of the assessment of seismic hazard as well as a comparison with the conventional Newmark

71 analysis.

72

73 **2 Study area**

74 The epicenter of the 2014 M_w 6.1 (the United States Geological Survey) Ludian earthquake was located

75 in the southeastern margin of the Tibetan Plateau. A rectangular area lying immediately around the

76 epicenter containing dense concentrations of the induced landslides was chosen for study (Fig. 1). The

77 elevation of the area ranged from 785 m to 3,085 m above sea level. Three rivers—the Niulanjiang River,

78 Shaba River, and Longquan River—pass through the study area (Fig. 1). The topography ranges from flat

79 in the river valleys to nearly vertical in the slopes on the banks of the rivers. According to Chen et al.

80 (2015), Niulanjiang River flows from the southeast (SE) to the northwest (NW), and incises to a depth

81 between 1,200 m and 3,300 m, resulting in about 80% of the slopes having angles greater than 40°

82 distributed along the banks. The predominant geological units of the study area have an age that varies

83 from the Proterozoic to the Mesozoic, including dolomite, limestone, shale, sandstone, basalt, and slate

84 (Fig. 2).

85 An inventory of 1,416 landslides triggered by the 2014 Ludian earthquake (Fig. 1) was compiled by visual

86 inspection through comparisons between pre-earthquake satellite images obtained from Google Earth

87 (January 30, 2014) and 0.2-m high-resolution post-earthquake aerial images (August 7, 2014; data

88 provided by the Digital Mountain and Remote Sensing Applications Center, Institute of Mountain

89 Hazards and Environment, Chinese Academy of Sciences, and Beijing Anxiang Power Technology Co.,

90 LTD.). A majority of landslides triggered by the earthquake were shallow, flow-like landslides (shallower

91 than 3 m), developing in particularly dense concentrations along steeply incised river valleys. The total

92 area of these interpreted landslides was 7.01 km^2 within a study area of 705 km^2. A detailed study showed

93 that 846 of the mapped landslides were greater than 1,000 m^2 in area, occupying 6.74 km^2 and accounting

94 for 96.1% of the total area of landslides, of which 279 were greater in area than 5,000 m^2, occupying 5.37

95 km^2 and accounting for 76.6% of the total landslide area.

96

97 **3 Methodology**

3.1 Modeling method

In the context of the analysis of the dynamic stability of a slope, Newmark (1965) proposed a permanent displacement analysis that bridges the gap between simplistic pseudostatic analysis and sophisticated, but generally impractical, finite element modeling (Jibson, 1993). Newmark's method simulates a landslide as a rigid plastic friction block with a known critical acceleration on an inclined plane (Fig. 3), and calculates the cumulative permanent displacement of the block as it is subjected to an acceleration-time history of an earthquake. Newmark (1965) showed that the dynamic stability of a slope is related to the critical acceleration of a potential landslide block, and can be expressed as a simple function of the static factor of safety and the geometry of the landslide (Jibson et al., 1998, 2000):

$$a_c = (F_S - 1)g\sin\alpha \tag{1}$$

where a_c is the critical acceleration in terms of g, the acceleration due to the Earth's gravity, F_S is the static factor of safety, and α is the angle from the horizontal at which the center of the slide block moves when displacement first occurs (Jibson et al., 1998, 2000). For a planar slip surface parallel to the slope, this angle generally approximates to the angle of the slope.

Natural slopes often develop a group of shallow unloading joints (Fig. 4) parallel to the surface due to valley incisions (Gu, 1979; Hoek and Bray, 1981). Studies have shown that rock slopes behave as collapsing and sliding failures of shallow unloading joints under strong earthquakes, and 90% of coseismic landslides are shallow falls and slides (Harp and Jibson, 1996; Khazai and Sitar, 2003; Dai et al., 2011; Tang et al., 2015). According to Qi et al. (2012), two typical kinds of landslides are triggered by earthquakes, i.e., (a) shallow, flow-like landslides with depth less than 3 m in general, and (b) rock falls thrown by the shaking caused by the earthquake, usually occurring at the crest of the slope. For both

118   types, unstable blocks of rock are often cut and activated along the rock joints. Therefore, the static factor

119   of safety in terms of the critical acceleration in these conditions is related to the peak shear strength of the

120   rock joints. For the purpose of regional analysis, we use a limit-equilibrium model of an infinite slope

121   (Fig. 3) by referring to the simplification of Newmark's method by of Jibson et al. (1998, 2000). The

122   value of the static factor of safety against sliding given by the ratio of resistance to the driving forces is

123   determined by conventional analysis without considering accelerations, expressed as:

$$F_S = \frac{Resisting\ force}{Driving\ force} = \frac{\tau L}{mg sin\alpha} = \frac{\tau L}{\gamma Lt sin\alpha} = \frac{\tau}{\gamma t sin\alpha} \tag{2}$$

124   where τ is the peak shear strength of the rock joint, L is the length of the rock joint, m is the mass of

125   the failure rock block, γ is the unit weight of the rock mass, and t is the thickness of the failure rock

126   block.

127   For a Newmark analysis, it is customary to describe the shear strength of rocks instead of rock joints in

128   terms of Coulomb's constants—friction angle (φ) and cohesion (c). However, both are not only stress

129   dependent, but also scale dependent (Barton and Choubey, 1977). According to Barton (1973), a more

130   satisfactory empirical relationship for predicting the peak shear strength of a joint can be written as

131   follows:

$$\tau = \sigma_n \tan\left[JRC\ log_{10}\left(\frac{JCS}{\sigma_n}\right) + \phi_b\right] \tag{3}$$

132   where σ_n is the effective normal stress, JRC is the joint roughness coefficient, JCS is the joint wall

133   compressive strength, and ϕ_b is the basic friction angle—the angle of frictional sliding resistance

134   between rock joints—which can be obtained from residual shear tests on natural joints (Barton, 1973).

135   The effective normal stress (σ_n) generated by gravity acting on the rock block is as follows:

$$\sigma_n = \frac{mgcos\alpha}{L} = \frac{\gamma Ltcos\alpha}{L} = \gamma tcos\alpha \tag{4}$$

136   Considering the impact of size on JRC and JCS, the formulations developed by Barton and Bandis (1982)

137   are shown as below:

$$JRC_n = JRC_0 \left(\frac{L_n}{L_0}\right)^{-0.02JRC_0} \tag{5}$$

$$JCS_n = JCS_0 \left(\frac{L_n}{L_0}\right)^{-0.03JRC_0} \tag{6}$$

138   where the nomenclature adopted incorporates (0) and (n) for values of the laboratory scale and the in-situ

139   scale, respectively.

140   Hence, the static factor of safety (F_S) of a slope can be written as:

$$F_S = \frac{\tau}{\gamma tsin\alpha} = \frac{\sigma_n tan\, [JRC_n\, log_{10}\left(\frac{JCS_n}{\sigma_n}\right) + \phi_b]}{\gamma tsin\alpha}$$

$$= \frac{\gamma tcos\alpha tan\, [JRC_n\, log_{10}\left(\frac{JCS_n}{\gamma tcos\alpha}\right) + \phi_b]}{\gamma tsin\alpha}$$

$$= \frac{tan\, [JRC_n\, log_{10}\left(\frac{JCS_n}{\gamma tcos\alpha}\right) + \phi_b]}{tan\alpha} \tag{7}$$

141   After calculating the angle of the slope and static factor of safety, the critical acceleration of the slope can

142   be determined. Once the time history of the earthquake' acceleration has been selected, portions of the

143   record lying above the critical acceleration a_c (Fig. 5a) are integrated once to derive a velocity profile

144 (Fig. 5b); the time history of velocity is then integrated a second time to obtain the profile of cumulative

145 displacement of the block (Fig. 5c). Users finally determine the dynamic performance of the slope based

146 on the magnitude of the Newmark displacement (Jibson et al., 1998, 2000; Jibson, 2011). The detailed

147 procedure of conducting a Newmark analysis with the Barton model is discussed in the following sections.

148 **3.2 Static factor-of-safety map**

149 Considering that the mapped landslides greater in area than 1,000 m^2 occupied 96.1% of the total landslide

150 area, we selected a 30 m × 30 m digital elevation model (DEM) from the ASTER Global Digital Elevation

151 Model (https://doi.org/10.5067/ASTER/ASTGTM.002, last accessed July 16, 2018), which facilitated the

152 subsequent hazard analysis. A basic slope algorithm was applied to the DEM to produce a slope map (Fig.

153 6), where the slope was identified as the steepest downhill descent from a cell to its neighbors (Burrough

154 and McDonell, 1998). The slopes ranged from greater than 60° along the banks of the Niulanjiang River,

155 Shaba River, and Longquan River, to less than 20° in low mountains and hills in the north and east.

156 According to Jibson et al. (1998, 2000), slopes steeper than 60° remain unstable even at high strengths.

157 We assume that Newmark's rigid plastic block is unsuitable for such a steep sliding surface. In this case,

158 sliding occurs along a plane at an angle (α) of $45°+\frac{\phi_b}{2}$ with the horizon (Fig. 7). Therefore, we assigned

159 an angle (α) of $45°+\frac{\phi_b}{2}$ to slopes steeper than 60° to avoid too small a value of F_S in the Newmark

160 analysis.

161 The digital geological map from the China Geological Survey (CGS) was rasterized at a 30-m grid spacing

162 to assign material properties throughout the study area. According to the literature, JRC_0 and JCS_0

163 depend strongly on lithology (Coulson, 1972; Barton and Choubey, 1977; Bandis et al., 1983; Bilgin and

164   Pasamehmetoglu, 1990; Priest, 1993; Singh et al., 2012; Alejano et al., 2012, 2014; Giusepone, 2014;

165   Yong et al., 2018). Representative values of γ, JRC_0, JCS_0, and ϕ_b assigned to each rock type exposed

166   in the study area were estimated using the test data listed in Table 1. The selected values were near the

167   middle of the ranges represented in the references. These JRC_0 and JCS_0 values were considered in a

168   laboratory scale for a length of 100 mm as L_0. For each grid cell in the regional analysis, the length of

169   the engineering dimension, L_n, can generally be set as a 10-fold range of L_0. This is because the value

170   of JRC_n/JRC_0 (JCS_n/JCS_0) is nearly constant when the value of L_n/L_0 is greater than 10 (Bandis et al.,

171   1981). The values of JRC_n and JCS_n, then, were calculated by inserting the values of JRC_0 and JCS_0,

172   and L_0, and L_n into Eqs. (5) and (6), respectively. Figures 8 and 9 show the spatial distributions of JRC_n

173   and JCS_n, respectively. The basic-friction-angle (ϕ_b) map and unit-weight (γ) map are shown in Figs. 10

174   and 11, respectively.

175   For the sake of simplicity, the thickness of the modeled block t was taken to be 3 m, which reflected the

176   typical slope failures of the Ludian earthquake. The static factor-of-safety map was produced by

177   combining these data layers (α, JRC_n, JCS_n, ϕ_b, and γ) in Eq. (7). In the initial iteration of the

178   calculation, grid cells in steep areas with static factors of safety smaller than one indicated that the slopes

179   were statically unstable, but did not necessarily mean that they were moving under shaking induced by

180   the earthquake. In this condition, to avoid conservative results, we neither increased the strengths of the

181   rock types with statically unstable cells nor adjusted the strengths of other rock types to preserve the

182   differences in relavtive strength between them (as in Jibson et al., 1998, 2000). Instead, we assigned a

183   minimal static factor of safety of 1.01, merely above limit equilibrium (Jibson et al., 1998, 2000), to these

184   slopes to avoid a negative value of the critical acceleration a_c. According to Keefer (1984), most

185 landslides triggered by earthquakes occur with a slope of at least 5°. The static factors of safety resulting

186 from slopes of angles smaller than 5° were very high. These slopes were unlikely to fail under the Ludian

187 earthquake, and did not produce a statistically significant sample in the analysis. Therefore, slopes less

188 steep than 5° were not analyzed in the second iteration. After the adjustment, the static factors of safety

189 ranged from 1 to 17.4, as shown in Fig. 12.

190 **3.3 Critical acceleration map**

191 According to Newmark (1965), a pseudostatic analysis in terms of the static factor of safety and the slope

192 angle was employed to calculate the critical acceleration of a potential landslide. The map of critical

193 acceleration (Fig. 13) was generated by combining the static factor of safety and the slope angle in Eq.

194 (1). The critical accelerations were derived from the intrinsic properties of the slope (topography and

195 lithology), regardless of the given shaking. Therefore, the map of critical acceleration indicated the

196 susceptibility of coseismic landslides (Jibson et al., 1998, 2000). The calculated critical accelerations

197 ranged from nearly zero in areas that were more susceptible to coseismic landslides to greater than 1 g

198 in areas that were less susceptibility.

199 **3.4 Shake map**

200 There were 23 strong-motion stations within 100 km of the epicenter of the Ludian earthquake (Fig. 14).

201 Each station's record contained the three components of the peak ground acceleration (PGA), south–north

202 direction, east–west direction, and up–down direction, as listed in Table 2 (the dataset was provided by

203 the China Earthquake Data Center, http://data.earthquake.cn, last accessed June 16, 2016). We calculated

204 the average PGA of the two horizontal components of each strong-motion recording and plotted a

205 contour map (Fig. 15) using an inverse distance-weighted (IDW) interpolation algorithm. It determined

206   the cell values using a linearly weighted combination of a set of sample stations with weights inversely

207   proportional to distance (Watson and Philip, 1985). In addition, given that input stations far from the

208   epicenter, where the prediction was made, might have had poor or no spatial correlation, we eliminated

209   the input stations beyond 100 km from the epicenter from the calculation.

210   **3.5 Newmark displacement map**

211   In case of a landslide in practice, it is impossible to conduct a rigorous Newmark analysis when

212   accelerometer records are unavailable. It is also impractical and time consuming to produce a

213   displacement in each cell during the regional analysis. Therefore, empirical regressions (Ambraseys and

214   Menu, 1988; Bray and Travasarou, 2007; Jibson, 2007; Saygili and Rathje, 2008; Rathje and Saygili,

215   2009; Hsieh and Lee, 2011) have been proposed to estimate Newmark displacement as a function of the

216   critical acceleration and peak ground acceleration, or the Arias intensity. Rathje and Saygili (2009)

217   developed a vector model for displacement in terms of the critical acceleration (a_c), peak ground

218   acceleration (PGA), and moment magnitude (M_w) based on an analysis of over 2,000 strong motion

219   recordings:

$$lnD = 4.89 - 4.85\left(\frac{a_c}{PGA}\right) - 19.64\left(\frac{a_c}{PGA}\right)^2 + 42.49\left(\frac{a_c}{PGA}\right)^3 - 29.06\left(\frac{a_c}{PGA}\right)^4$$

$$+0.72\ln(PGA) + 0.89(M_w - 6) \tag{8}$$

220   where D is the predicted displacement in units of cm, and a_c and PGA are in units of g.

221   This model is a preferred displacement model at a site where acceleration-time recordings are not

222   available. Incorporating multiple parameters of ground motion into the analysis typically results in less

223   variation in the prediction of displacement (Rathje and Saygili, 2009).

224 The Newmark displacement of each cell was calculated by combining the corresponding values of the

225 critical acceleration, peak ground acceleration, and moment magnitude in Eq. (8). The predicted

226 displacements ranged from 0 cm to 122 cm, as shown in Fig. 16.

3.6 Coseismic landslide hazard map

228 According to Jibson et al. (1998, 2000), predicted displacements provide an index of the seismic

229 performance of slopes, where larger predicted displacements relate to a greater incidence of slope failures.

230 But the displacements do not correspond directly to measurable slope movements in the field. To produce

231 a coseismic landslide hazard map, we chose a model of inexact reasoning, the certainty factor model

232 (CFM), created by Shortliffe and Buchanan (1975) and improved by Hecherman (1986), to explore the

233 relationship between the occurrences of landslides and their predicted displacements. The CFM was

234 created as a numerical method, initially used in MYCIN, a backward-chaining expert system in medicine

235 (Shortliffe and Buchanan, 1975), for managing uncertainty in a rule-based system. In this model, the

236 certainty factor CF represents the net confidence in a hypothesis H based on the evidence E

237 (Hecherman, 1986). Certainty factors range between -1 and 1. A CF with a value of -1 means a total lack

238 of confidence, whereas a CF with a value of 1 means total confidence. Values greater than zero favor

239 the hypothesis while those less than zero favor its negation. According to Hecherman (1986), the

240 probabilistic interpretation of CF is as follows:

$$CF = \begin{cases} \dfrac{p(H|E) - p(H)}{p(H|E)[1 - p(H)]}, & p(H|E) > p(H) \\[4mm] \dfrac{p(H|E) - p(H)}{p(H)[1 - p(H|E)]}, & p(H|E) < p(H) \end{cases} \qquad (9)$$

241   where CF is the certainty factor, $p(H|E)$ denotes the conditional probability for a posterior hypothesis

242   that relies on evidence, the posterior probability, and $p(H)$ is the prior probability before any evidence

243   is known. In the displacement analysis, $p(H|E)$ was defined as the proportion of the area of the landslide

244   within a specific displacement area, and $p(H)$ was defined as the proportion of the landslide area within

245   the entire study area, excluding slopes less steep than 5°. In this way, the values of CF represented the

246   confidence level for coseismic landslides. Positive values corresponded to an increase in the confidence

247   level in slope failure while negative quantities corresponded to a decrease in this confidence. Higher

248   positive values indicated higher confidence levels for coseismic landslides.

249   Given the above definition, we produced a coseismic landslide hazard map in terms of the certainty factors.

250   First, displacement cells every 1 cm were grouped into bins such that all cells with displacements between

251   0 cm and 1 cm were grouped into the first bin, those with displacements between 1 cm and 2 cm were

252   grouped into the second bin, and so on. The displacements were grouped into 123 bins, from 0 cm to 122

253   cm. We then calculated the proportion of cells occupied by areas of landslides in each bin. This proportion

254   was considered the posterior probability of each bin as defined. The prior probability calculated by

255   dividing the entire landslide area by the entire study area was the same in each bin. Finally, the values of

256   CF were computed in each bin by using Eq. (9) to combine the corresponding values of the posterior and

257   prior probabilities. The certainty factors ranged from -1 to 0.95. The values of CF indicated the

258   confidence level of the occurrence of a landslide for each bin in the study area, and provided the basis for

259   producing the coseismic landslide hazard map.

260   As shown in the hazard map (Fig. 17), 73.2% of landslides triggered by the Ludian earthquake were in

261   areas with higher confidence levels, with CF values greater than 0.6. The interpreted landslides were

262   covered on the map to demonstrate their goodness of fit for the predicted confidence levels for coseismic

263   landslides (Fig. 17).

264

265   **4 Results and discussion**

266   The predicted displacements represent the cumulative sliding displacements for a given time history of

267   acceleration. Based on the statistically significant sizes of the areas, displacements less than 60 cm, which

268   was around the middle of the range of displacement, occupied about 80% of the study area while

269   displacements greater than 80 cm occupied a very small area. Jibson et al. (1998, 2000) assumed that

270   shallow falls and slides in brittle, weakly cemented materials fail at a relatively small displacement,

271   whereas slumps and block slides in more compliant materials likely fail at a larger displacement. That is

272   to say, the study area was more susceptible to rock falls and shallow, disrupted slides that fail at a relatively

273   small displacement. By contrast, it was subjected with a lower probability to coherent, deep-seated slides

274   that would fail at a larger displacement. Indeed, the majority of landslides triggered by the Ludian

275   earthquake were shallow, disrupted slides and rock falls (Zhou et al., 2016). Although a few catastrophic

276   rock avalanches, such as the Hongshiyan landslide (Chang et al., 2017), occurred in the field, they did not

277   produce statistically significant samples that could meaningfully contribute to the model, which is

278   consistent with the statistical results as discussed above. Therefore, the model should relate well to typical

279   kinds of earthquake-induced landslides in the study area, thus demonstrating its usefulness in predicting

280   the probability of other types of landslides.

281   According to Jibson et al. (1998, 2000), a function of CF and Newmark displacement would make it

282   possible to predict the spatial variation in coseismic landslides in any scenario of interest involving the

283   ground shaking. As mentioned above, 80% of the study area featured predicted displacements of less than

284   60 cm. The numbers of the Newmark displacement cells were uneven. There were more cells in 1 cm bins

285   for smaller displacements and fewer cells in 1 cm bins for larger ones. This might have affected the

286   statistical significance of the function of CF and Newmark displacement. Therefore, the predicted

287   displacement cells were grouped into bins based on quantile statistics. The breakpoints were 0, 10, 30, 39,

288   46, 51, 55, 59, 63, and 122. In this way, the number of cells in each bin was equal. Figure 18 shows, in

289   each bin, the CF value of the Newmark displacement as plotted as a dot. As CF values ranged from -1

290   to 1, and not from 0 to 1, the Weibull (1939) curve developed by Jaeger and Cook (1969) is unsuitable

291   here. Therefore, we modified the functional form as below:

$$CF = 2k[1 - exp(-aD^b)] - 1 \qquad (10)$$

292   where CF is the certainty factor, k is the maximum CF value represented by the data, D is predicted

293   displacement, and a and b are regression constants. The regression curve based on data from the

294   Ludian earthquake is

$$CF = 1.837[1 - exp(-0.073D^{0.821})] - 1 \qquad (11)$$

295   From the curve shown in Fig. 18, when the predicted displacement increased, the value of CF increased

296   monotonically, meaning that the confidence level for slope failure grew and landslide would probably

297   occur. Such a procedure is consistent with the interpretation of certainty factor theory. Therefore, we were

298   able to obtain estimates of the hazard different from the one used in this study using the same procedure

299   described here.

300   When fitting the results of shear tests using Coulomb's linear relation, the shear strengths varied widely

301   from high normal stress in the laboratory to low normal stress in the field (Barton, 1973). We introduced

302   the Barton model to the Newmark analysis to reduce the variation in shear strength in terms of Coulomb's

303   constants. We also considered the impact of scale effects by using Eqs. (5) and (6) to prevent Newmark's

304   method from underestimating the shear strength of geological units in regional analysis. In addition, for

305   the Barton model, the joint roughness coefficient (JRC) was estimated from tilt tests, or by matching

306   Barton's joint standard roughness profiles regarded by the International Society for Rock Mechanics

307   (ISRM, 1978). The joint wall compressive strength (JCS) was estimated by Schmidt hammer index tests.

308   These tests helped make a quick estimate of the shear strength in situ, which can facilitate the use of

309   Newmark's method in an emergency hazard and risk assessment after an earthquake.

310   It is difficult for a statically stable slope to fail under an earthquake. Earthquakes usually cause slopes to

311   fail in the state of limit equilibrium. For this reason, it is important to characterize the shear strength of

312   the slope accurately. The shear strengths were assigned to the geological units using the results of

313   hundreds of shear tests reported in the references provided in Table 1. We assigned the original shear

314   strengths to the geological units, instead of increasing them to render the cells statically stable, as Jibson

315   et al. (1998, 200) did. This would have changed the statically stable level of the entire study area,

316   especially the slopes in the state of limit equilibrium. In addition, we considered the size effect of the

317   potential slide surface, which could yield a lower F_S and, in turn, a higher displacement. However, the

318   inventory of landslides was used to calibrate the predicted displacements, and the confidence levels

319   indicated by the certainty factors fitted well with the spatial distribution of coseismic landslides, as shown

320   in the hazard map (Fig. 17).

321   We also ran a conventional Newmark analysis using the assigned strengths, such as friction angle (φ) and

322   cohesion (c), as shown in Table 2. The predicted displacements calculated by the conventional Newmark

323   analysis ranged from 0 cm to 121 cm, compared with 0 cm to 122 cm as obtained by the proposed method.

324   Figure 19 shows the hazard map produced using conventional Newmark analysis. The CFs ranged from

325   -1 to 0.94, indicating a very similar result to that of the proposed method above. However, there were

326   large differences along the Shaba River and upstream of the Niulanjiang River between the methods. By

327   comparing Fig. 17 with Fig. 19, we see that the confidence levels of the proposed method fitted the data

328   better than those of the conventional method, especially near upstream of the Niulanjiang River. The area

329   under the curve (AUC) was employed to compare the performance of the methods. To create an AUC

330   plot, the cumulative area of CFs within each interval of the calculated values, from the maximum to the

331   minimum, was determined as a proportion of the total study area (x-axis) and plotted against the

332   proportion of cumulative landslides falling within those CFs (y-axis) (Miles and Keefer, 2009). A value

333   of 0.5 of the AUC indicates that performance is not better than a random guess and that of 1 indicates

334   perfect performance (Miles and Keefer, 2009). Figure 20 shows the results of the AUC analysis of both

335   methods. The calculated value for the proposed method was 0.58 while that for the conventional

336   Newmark's method was 0.53. That is to say, the method introduced here yielded better results, and is an

337   improvement over the conventional Newmark analysis.

338

339   **5 Conclusion**

340   Newmark's method is a useful physical model to estimate the seismic stability of natural slopes. The

341   mapping procedure for data on the 2014 Ludian earthquake shows the feasibility of a Newmark analysis

342   combined with Barton's shear strength criterion. Such a method has practical applications in the

343   assessment of regional seismic hazard. We also considered here the size effect of parameters of shear

344   strength, such as the joint roughness coefficient (JRC) and the joint wall compressive strength (JCS), in

345   regional analysis. Moreover, linking the Newmark displacements to the certainty factor model improved

346   the utility of Newmark's method to predict the hazard posed by coseismic landslides. Finally, the results

347   of an AUC analysis indicate that the proposed method is more reliable than the conventional Newmark's

348   method.

349

350   Data availability. The digital geological map hosted by the China Geological Survey (CGS) can be made

351   available upon request. The pre-earthquake satellite images are publicly available from Google Earth (last

352   access: 30 January 2014). The 0.2-m high-resolution post-earthquake aerial images from the Digital

353   Mountain and Remote Sensing Applications Center, Institute of Mountain Hazards and Environment,

354   Chinese Academy of Sciences, and Beijing Anxiang Power Technology Co., LTD. are restricted and

355   cannot be accessed publicly but may be requested from the corresponding author. The 30 m × 30 m

356   ASTER Global Digital Elevation Model is distributed by NASA EOSDIS Land Processes DAAC

357   (https://doi.org/10.5067/ASTER/ASTGTM.002, last access: 16 July 2018). The dataset of the strong-

358   motion stations is provided by the China Earthquake Data Center (http://data.earthquake.cn, last access:

359   16 June 2016).

360

361   Author contributions. SQ initiated and led this research. MZ designed the analytical framework of this

362   study, produced maps and figures, performed the data analysis and interpretation, and wrote the paper.

363   YZ helped interpret landslides and collect the records of the strong-motion stations. SQ, ZS, and BSZ

364   reviewed and edited the paper.

365

366   Competing interests. The authors declare that they have no conflict of interest.

367

368   Acknowledgements. This research was supported by the National Natural Science Foundation of China

369   (Grant Nos. 41825018, 41672307, and 41807273), the Science and Technology Service Network

370   Initiative (Grant No. KFJ-EW-STS-094), and the China Scholarship Council (No. 201704910537).

371

372   Review statement. This paper was edited by Mario Parise and reviewed by two anonymous referees.

373

References

Alejano, L. R., González, J. and Muralha, J.: Comparison of different techniques of tilt testing and basic friction angle variability assessment, Rock Mech. Rock Eng., 45, 1023-1035, https://xs.scihub.ltd/https://doi.org/10.1007/s00603-012-0265-7, 2012.

Alejano, L. R., Perucho, Á., Olalla, C. and Jiménez, R. (Eds.): Rock engineering and rock mechanics: structures in and on rock masses, CRC Press/Balkema, Leiden, the Netherlands, 1536 pp., 2014.

Ambraseys, N. N. and Menu, J. M.: Earthquake–induced ground displacements, Earthquake Eng. Struct. Dyn., 16, 985-1006, https://doi.org/10.1002/eqe.4290160704, 1988.

Bandis, S., Lumsden, A. C. and Barton, N. R.: Experimental studies of scale effects on the shear behaviour of rock joints, Int. J. Rock Mech. Min. Sci. & Geomech. Abstr., 18, 1-21, https://doi.org/10.1016/0148-9062(81)90262-X, 1981.

Bandis, S. C., Lumsden, A. C. and Barton, N. R.: Fundamentals of rock joint deformation, Int. J. Rock Mech. Min. Sci. & Geomech. Abstr., 20, 249-268, https://doi.org/10.1016/0148-9062(83)90595-8, 1983.

Barton, N.: Review of a new shear-strength criterion for rock joints, Eng. Geol., 7, 287-332, https://doi.org/10.1016/0013-7952(73)90013-6, 1973.

Barton, N. and Bandis, S.: Effects of block size on the shear behavior of jointed rock, in: Proceedings of the 23rd US Symposium on Rock Mechanics (USRMS), Berkeley, California, USA, 25-27 August 1982, 739-760, 1982.

Barton, N. and Choubey, V.: The shear strength of rock joints in theory and practice, Rock Mech., 10, 1-54, https://xs.scihub.ltd/https://doi.org/10.1007/BF01261801, 1977.

395 Bilgin, H. A. and Pasamehmetoglu, A. G.: Shear behaviour of shale joints under heat in direct shear, in:

396 Proceedings of the International symposium on rock joints, Leon, Norway, 4-6 June 1990, 179-183,

397 1990.

398 Bray, J. D. and Travasarou, T.: Simplified procedure for estimating earthquake-induced deviatoric slope

399 displacements, J. Geotech. Geoenviron., 133, 381-392, https://doi.org/10.1061/(ASCE)1090-

400 0241(2007)133:4(381), 2007.

401 Burrough, P. A. and McDonnell, R. A. (Eds.): Principles of geographical information systems (2nd

402 Edition), Oxford University Press, Oxford, UK, 1998.

403 Chang, Z. F., Chang, H., Yang, S. Y., Chen, G. and Li, J. L.: Characteristics and formation mechanism

404 of large rock avalanches triggered by the Ludian Ms6.5 earthquake at Hongshiyan and Ganjiazhai,

405 Seismology and Geology, 39, 1030-1047, 2017 (in Chinese with English abstract).

406 Chen, X. L., Ran, H. L. and Yang, W. T.: Evaluation of factors controlling large earthquake-induced

407 landslides by the Wenchuan earthquake, Nat. Hazards Earth Syst. Sci., 12, 3645-3657,

408 https://doi.org/10.5194/nhess-12-3645-2012, 2012.

409 Chen, X. L., Zhou, Q. and Liu, C. G.: Distribution pattern of coseismic landslides triggered by the 2014

410 Ludian, Yunnan, China Mw6.1 earthquake: special controlling conditions of local topography,

411 Landslides, 12, 1159-1168, https://xs.scihub.ltd/https://doi.org/10.1007/s10346-015-0641-y, 2015.

412 Chen, X. L., Liu, C. G., Wang, M. M. and Zhou, Q.: Causes of unusual distribution of coseismic landslides

413 triggered by the Mw 6.1 2014 Ludian, Yunnan, China earthquake, J. Asian Earth Sci., 159, 17-23,

414 https://doi.org/10.1016/j.jseaes.2018.03.010, 2018.

Chen, X. L., Liu, C. G. and Wang, M. M.: A method for quick assessment of earthquake-triggered landslide hazards: a case study of the Mw6. 1 2014 Ludian, China earthquake, Bull. Eng. Geol. Environ., 78, 2449-2458, https://xs.scihub.ltd/https://doi.org/10.1007/s10064-018-1313-7, 2019.

China Earthquake Data Center: http://data.earthquake.cn, last access: 16 June 2016.

Clough, R. W. and Chopra, A. K.: Earthquake stress analysis in earth dams, ASCE J. Eng. Mech. Div., 92, 197-211, 1966.

Coulson, J. H.: Shear strength of flat surfaces in rock, in: Proceedings of the 13th Symposium on Rock Mechanics, Urbana, Illinois, USA, August 30-September 1, 1971, 77-105, 1972.

Dai, F. C., Xu, C., Yao, X., Xu, L., Tu, X. B. and Gong, Q. M.: Spatial distribution of landslides triggered by the 2008 Ms 8.0 Wenchuan earthquake, China, J. Asian Earth Sci., 40, 883-895, https://doi.org/10.1016/j.jseaes.2010.04.010, 2011.

Geological Engineering Handbook Editorial Committee (Ed.): Geological Engineering Handbook, China Architecture & Building Press, Beijing, China, 2018 (in Chinese).

Giusepone, F. and da Silva, L. A. A.: Hoek & Brown and Barton & Bandis Criteria Applied to a Planar Sliding at a Dolomite Mine in Gandarela Synclinal, in: Proceedings of the ISRM Conference on Rock Mechanics for Natural Resources and Infrastructure-SBMR 2014, Goiania, Brazil, 9-13 September 2014, ISRM-SBMR-2014-009, 2014.

Gu, D. Z. (Ed.): Engineering geomechanics of rock mass, Science Press, Beijing, China, 1979 (in Chinese).

Harp, E. L. and Jibson, R. W.: Landslides triggered by the 1994 Northridge, California, earthquake, Bull. Seismol. Soc. Am., 86, S319-S332, 1996.

435   Heckerman, D.: Probabilistic interpretations for MYCIN's certainty factors, Mach. Intell. Patt. Rec., 4,

436   167-196, https://doi.org/10.1016/B978-0-444-70058-2.50017-6, 1986.

437   Hsieh, S. Y. and Lee, C. T.: Empirical estimation of the Newmark displacement from the Arias intensity

438   and critical acceleration, Eng. Geol., 122, 34-42, https://doi.org/10.1016/j.enggeo.2010.12.006, 2011.

439   Hoek, E. and Bray, J. D. (Eds.): Rock slope engineering (3rd editon), Taylor & Francis, Abingdon, UK,

440   1981.

441   International Society for Rock Mechanics (ISRM): International society for rock mechanics commission

442   on standardization of laboratory and field tests: Suggested methods for the quantitative description

443   of discontinuities in rock masses, Int. J. Rock Mech. Min. Sci. & Geomech. Abstr., 15, 319-368,

444   https://doi.org/10.1016/0148-9062(78)91472-9, 1978.

445   Jaeger, J. C. and Cook, N. G. W. (Eds.): Fundamentals of Rock Mechanics, Methuen, London, UK, 513

446   pp., 1969.

447   Jibson, R. W.: Predicting earthquake-induced landslide displacements using Newmark's sliding block

448   analysis, Transp. Res. Rec., 1411, 9-17, 1993.

449   Jibson, R. W.: Regression models for estimating coseismic landslide displacement, Eng. Geol., 91, 209-

450   218, https://doi.org/10.1016/j.enggeo.2007.01.013, 2007.

451   Jibson, R. W.: Methods for assessing the stability of slopes during earthquakes-A retrospective, Eng.

452   Geol., 122, 43-50, https://doi.org/10.1016/j.enggeo.2010.09.017, 2011.

453   Jibson, R. W., Harp, E. L. and Michael, J. A.: A method for producing digital probabilistic seismic

454   landslide hazard maps: an example from the Los Angeles, California, area, U.S. Geological Survey,

455   Denver, USA, Open File Rep. 98-113, 17 pp., 1998.

456   Jibson, R. W., Harp, E. L. and Michael, J. A.: A method for producing digital probabilistic seismic

457   landslide hazard maps, Eng. Geol., 58, 271-289, https://doi.org/10.1016/S0013-7952(00)00039-9,

458   2000.

459   Keefer, D. K.: Landslides caused by earthquakes, Geol. Soc. Am. Bull., 95, 406-421,

460   https://doi.org/10.1130/0016-7606(1984)95<406:LCBE>2.0.CO;2, 1984.

461   Khazai, B. and Sitar, N.: Evaluation of factors controlling earthquake-induced landslides caused by Chi-

462   Chi earthquake and comparison with the Northridge and Loma Prieta events, Eng. Geol., 71, 79-95,

463   https://doi.org/10.1016/S0013-7952(03)00127-3, 2004.

464   Miles, S. B. and Keefer, D. K.: Evaluation of CAMEL-comprehensive areal model of earthquake-induced

465   landslides, Eng. Geol., 104, 1-15, https://doi.org/10.1016/j.enggeo.2008.08.004, 2009.

466   NASA/METI/AIST/Japan Spacesystems, and U.S./Japan ASTER Science Team: ASTER Global Digital

467   Elevation   Model   version   002,   NASA   EOSDIS   Land   Processes   DAAC,

468   https://doi.org/10.5067/ASTER/ASTGTM.002, 2009.

469   Newmark, N. M.: Effects of earthquakes on dams and embankments, Geotechnique, 15, 139-160, 1965.

470   Pradel, D., Smith, P. M., Stewart, J. P. and Raad, G.: Case history of landslide movement during the

471   Northridge   earthquake,   J.   Geotech.   Geoenviron.   Eng.,   131,   1360-1369,

472   https://doi.org/10.1061/(ASCE)1090-0241(2005)131:11(1360), 2005.

473   Priest, S. D. (Ed.): Discontinuity analysis for rock engineering, Chapman & Hall, London, UK, 1993.

474   Qi, S. W., Xu, Q., Lan, H. X., Zhang, B. and Liu, J. Y.: Spatial distribution analysis of landslides triggered

475   by   2008.5.12   Wenchuan   Earthquake,   China,   Eng.   Geol.,   116,   95-108,

476   https://doi.org/10.1016/j.enggeo.2010.07.011, 2010.

Qi, S. W., Xu, Q., Zhang, B., Zhou, Y. D., Lan, H. X. and Li, L. H.: Source characteristics of long runout rock avalanches triggered by the 2008 Wenchuan earthquake, China, J. Asian Earth Sci., 40, 896-906, https://doi.org/10.1016/j.jseaes.2010.05.010, 2011.

Qi, S. W., Yan, C. G. and Liu, C. L.: Two typical types of earthquake triggered landslides and their mechanisms, in: Proceedings of the 11th International and 2nd North American Symposium on Landslides and Engineered Slopes, Banff, Canada, 3-8 June 2012, 1819-1823, 2012.

Rathje, E. M. and Antonakos, G.: A unified model for predicting earthquake-induced sliding displacements of rigid and flexible slopes, Eng. Geol., 122, 51-60, https://doi.org/10.1016/j.enggeo.2010.12.004, 2011.

Rathje, E. M. and Saygili, G.: Probabilistic assessment of earthquake-induced sliding displacements of natural slopes, Bulletin of the New Zealand Society for Earthquake Engineering, 42, 18-27, https://doi.org/10.5459/bnzsee.42.1.18-27, 2009.

Saygili, G. and Rathje, E. M.: Empirical predictive models for earthquake-induced sliding displacements of slopes, J. Geotech. Geoenviron. Eng., 134, 790-803, https://doi.org/10.1061/(ASCE)1090-0241(2008)134:6(790), 2008.

Shortliffe, E. H. and Buchanan, B. G.: A model of inexact reasoning in medicine, Math. Biosci., 23, 351-379, https://doi.org/10.1016/0025-5564(75)90047-4, 1975.

Singh, T. N., Kainthola, A. and Venkatesh, A.: Correlation between point load index and uniaxial compressive strength for different rock types, Rock Mech. Rock Eng., 45, 259-264, https://xs.scihub.ltd/https://doi.org/10.1007/s00603-011-0192-z, 2012.

497   Tang, C., Ma, G., Chang, M., Li, W., Zhang, D., Jia, T. and Zhou, Z.: Landslides triggered by the 20 April

498   2013 Lushan earthquake, Sichuan Province, China, Eng. Geol., 187, 45-55,

499   https://doi.org/10.1016/j.enggeo.2014.12.004, 2015.

500   Terzaghi, K.: Mechanism of landslides, in: Application of Geology to Engineering Practice, edited by:

501   Paige, S., Geological Society of America, New York, NY, USA, 83-123,

502   https://doi.org/10.1130/Berkey.1950.83, 1950.

503   Watson, D. F. and Philip, G. M.: A Refinement of Inverse Distance Weighted Interpolation,

504   Geoprocessing, 2, 315-327, 1985.

505   Weibull, W. (Ed.): A Statistical Theory of the Strength of Materials, Generalstabens Litografiska Anstalts

506   Förlag, Stockholm, Sweden, 1939.

507   Wieczorek, G. F., Wilson, R. C. and Harp, E. L.: Map showing slope stability during earthquakes in San

508   Mateo County, California, U.S. Geological Survey, Denver, USA, Map I-1257-E,

509   https://doi.org/10.3133/i1257E, 1985.

510   Wilson, R. C. and Keefer, D. K.: Dynamic analysis of a slope failure from the 6 August 1979 Coyote

511   Lake, California, earthquake, Bull. Seismol. Soc. Am., 73, 863-877, 1983.

512   Xu, C., Xu, X., Zhou, B., amd Yu, G.: Revisions of the M 8.0 Wenchuan earthquake seismic intensity

513   map based on co-seismic landslide abundance, Nat. Hazards, 69, 1459-1476,

514   https://xs.scihub.ltd/https://doi.org/10.1007/s11069-013-0757-0, 2013.

515   Yong, R., Ye, J., Liang, Q. F., Huang, M. and Du, S. G.: Estimation of the joint roughness coefficient

516   (JRC) of rock joints by vector similarity measures, Bull. Eng. Geol. Environ., 77, 735-749,

517   https://xs.scihub.ltd/https://doi.org/10.1007/s10064-016-0947-6, 2018.

518   Yuan, R. M., Tang, C. L., Hu, J. C., and Xu, X. W.: Mechanism of the Donghekou landslide triggered by

519   the 2008 Wenchuan earthquake revealed by discrete element modeling, Nat. Hazards Earth Syst.

520   Sci., 14, 1195-1205, https://doi.org/10.5194/nhess-14-1195-2014, 2014.

521   Zhou, S. H., Chen, G. Q. and Fang, L. G.: Distribution pattern of landslides triggered by the 2014 Ludian

522   earthquake of China: Implications for regional threshold topography and the seismogenic fault

523   identification, ISPRS Int. J. Geo-Inf., 5, 46, https://doi.org/10.3390/ijgi5040046, 2016.

524

525   **Figure Captions**

526   **Fig. 1.** Map of the study area showing the inventoried landslides.

527   **Fig. 2.** Geological map of the study area showing lithology and faults.

528   **Fig. 3.** Conceptual sliding-block model of Newmark analysis.

529   **Fig. 4.** A schematic diagram showing shadow unloading joints in the slope.

530   **Fig. 5.** Demonstration of the Newmark analysis algorithm (adapted from Wilson and Keefer, 1983; Jibson

531   et al., 1998, 2000)

532   **Fig. 6.** Slope map derived from the DEM of the study area.

533   **Fig. 7.** Schematic map showing the angle (α) for slopes steeper than 60°. σ_{1f} and σ_3 are the major

534   and minor principal stress in the state of limit equilibrium, respectively. ϕ_b is the basic friction angle.

535   **Fig. 8.** JRC_n component of shear strength assigned to rock types in the study area.

536   **Fig. 9.** JCS_n component of shear strength assigned to rock types in the study area.

537   **Fig. 10.** Basic-friction-angle (ϕ_b) component of shear strength assigned to rock types in the study area.

538   **Fig. 11.** Unit weight (γ) assigned to rock types in the study area.

539   **Fig. 12.** Static factor-of-safety map of the study area.

540   **Fig. 13.** Map showing critical accelerations in the study area.

541   **Fig. 14.** Locations of strong-motion stations.

542   **Fig. 15.** Contour map of peak ground acceleration (PGA) produced by the Ludian earthquake in the

543   study area. PGA values shown are in g.

544   **Fig. 16.** Map showing predicted displacements in the study area.

545   **Fig. 17.** Map showing confidence levels of coseismic landslides in the Ludian earthquake using the

546   proposed method. Confidence levels are portrayed in terms of values of CF.

547   **Fig. 18.** Proportion of the area of landslides in each CF value area. A dot shows the CF value of

548   Newmark displacement bin; the red line is the fitting curve of the data using a modified Weibull function.

549   **Fig. 19.** Map showing confidence levels of coseismic landslides in the Ludian earthquake using a

550   conventional Newmark analysis. Confidence levels are portrayed in terms of values of CF.

551   **Fig. 20.** Plots of area under the curve comparing the proposed method with the conventional Newmark's

552   method.

553
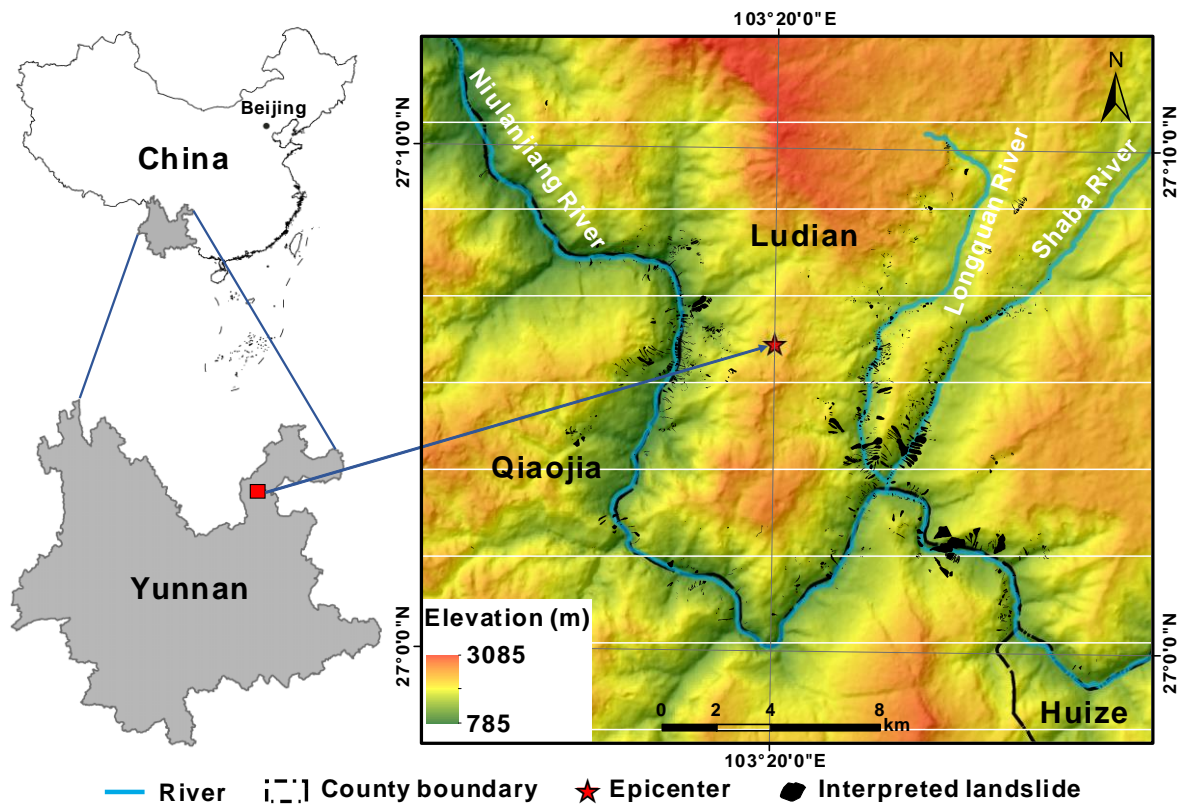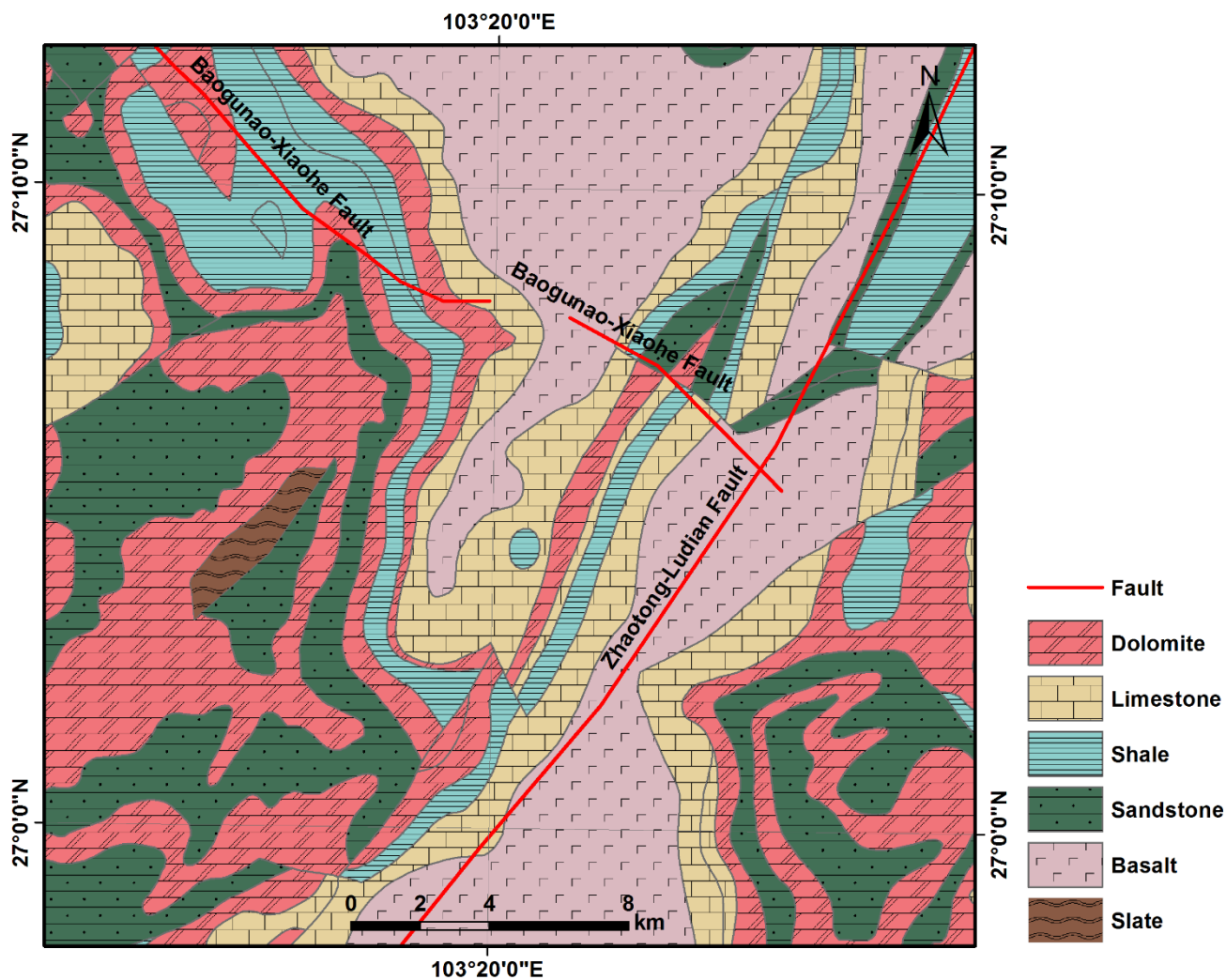
554   — River   ⌐ ⌐ County boundary   ★ Epicenter   ⬢ Interpreted landslide

555   **Fig. 1.** Map of the study area showing the inventoried landslides.

556

557

Fig. 2. Geological map of the study area showing lithology and faults.

559

560

561
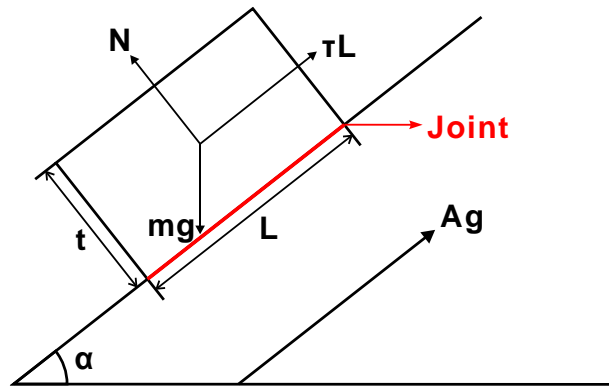
Fig. 3. Conceptual sliding-block model of Newmark analysis. The potential landslide is modeled as a

rigid plastic block resting on an inclined plane at an angle (α) from the horizontal (Jibson et al., 1998,

2000). The base of the block is subjected to an earthquake ground acceleration that is denoted by Ag.
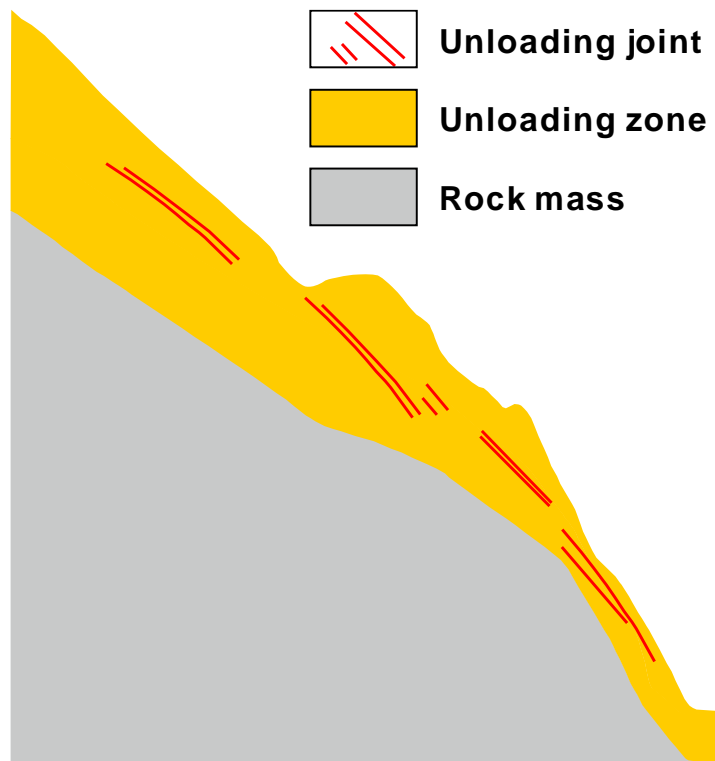
566

567 **Fig. 4.** A schematic diagram showing shallow unloading joints in the slope.

568
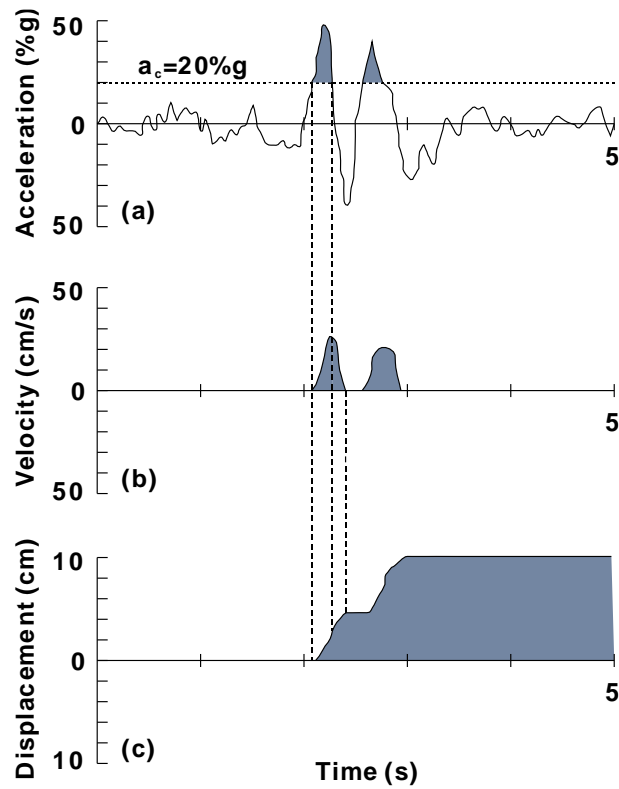
569

570   **Fig. 5.** Demonstration of the Newmark analysis algorithm (adapted from Wilson and Keefer, 1983; Jibson

571   et al., 1998, 2000): (a) Acceleration-time history with critical acceleration (horizontal dotted line) of 20%g

572   superimposed. (b) Velocity of block versus time. (c) Displacement of block versus time.

573

574
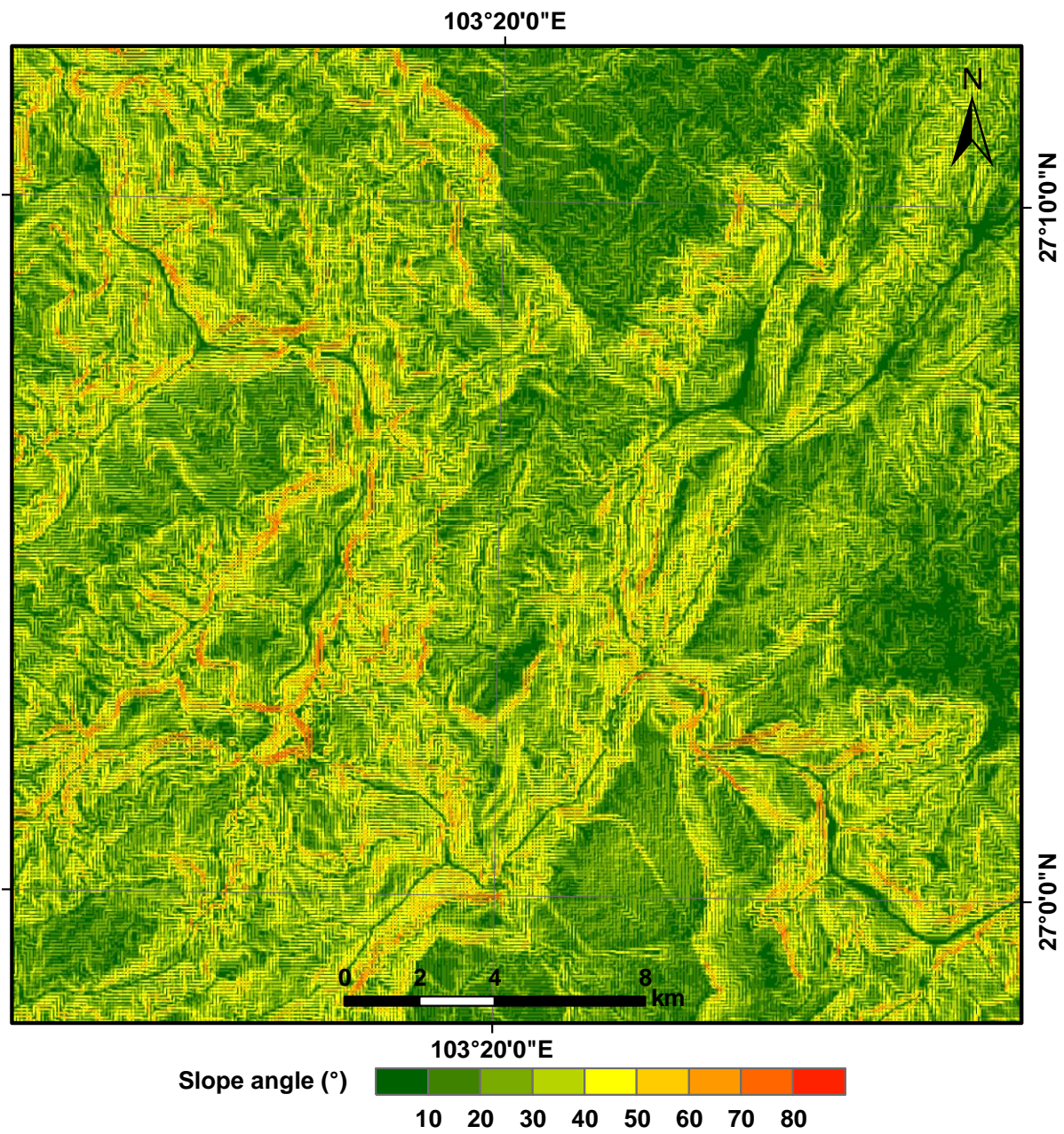
Fig. 6. Slope map derived from the DEM of the study area.

576
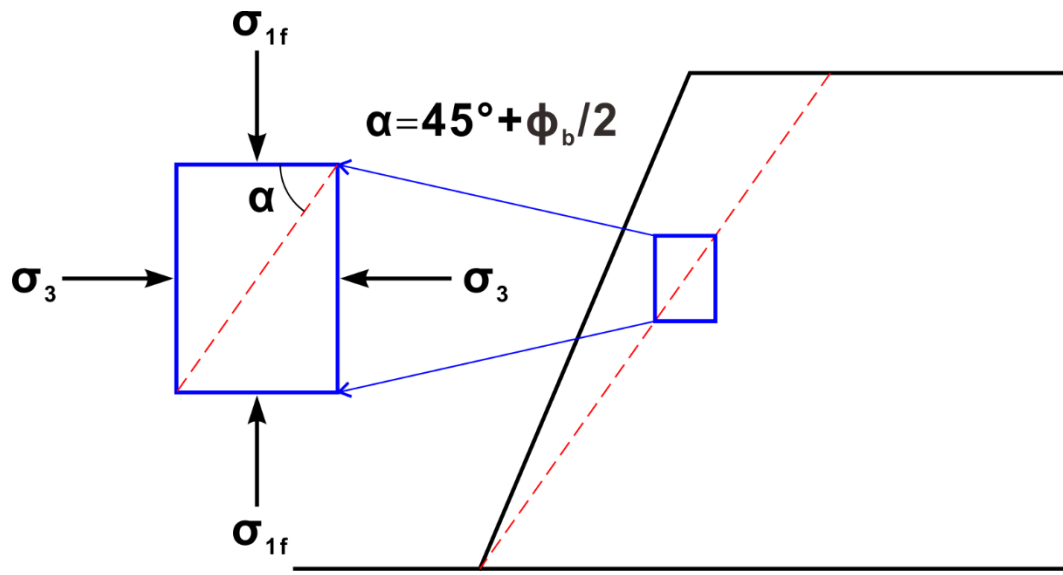
577

578 **Fig. 7.** Schematic map showing the angle (α) for slopes steeper than 60°. σ_{1f} and σ_3 are the major

579 and minor principal stress in the state of limit equilibrium, respectively. ϕ_b is the basic friction angle.

580
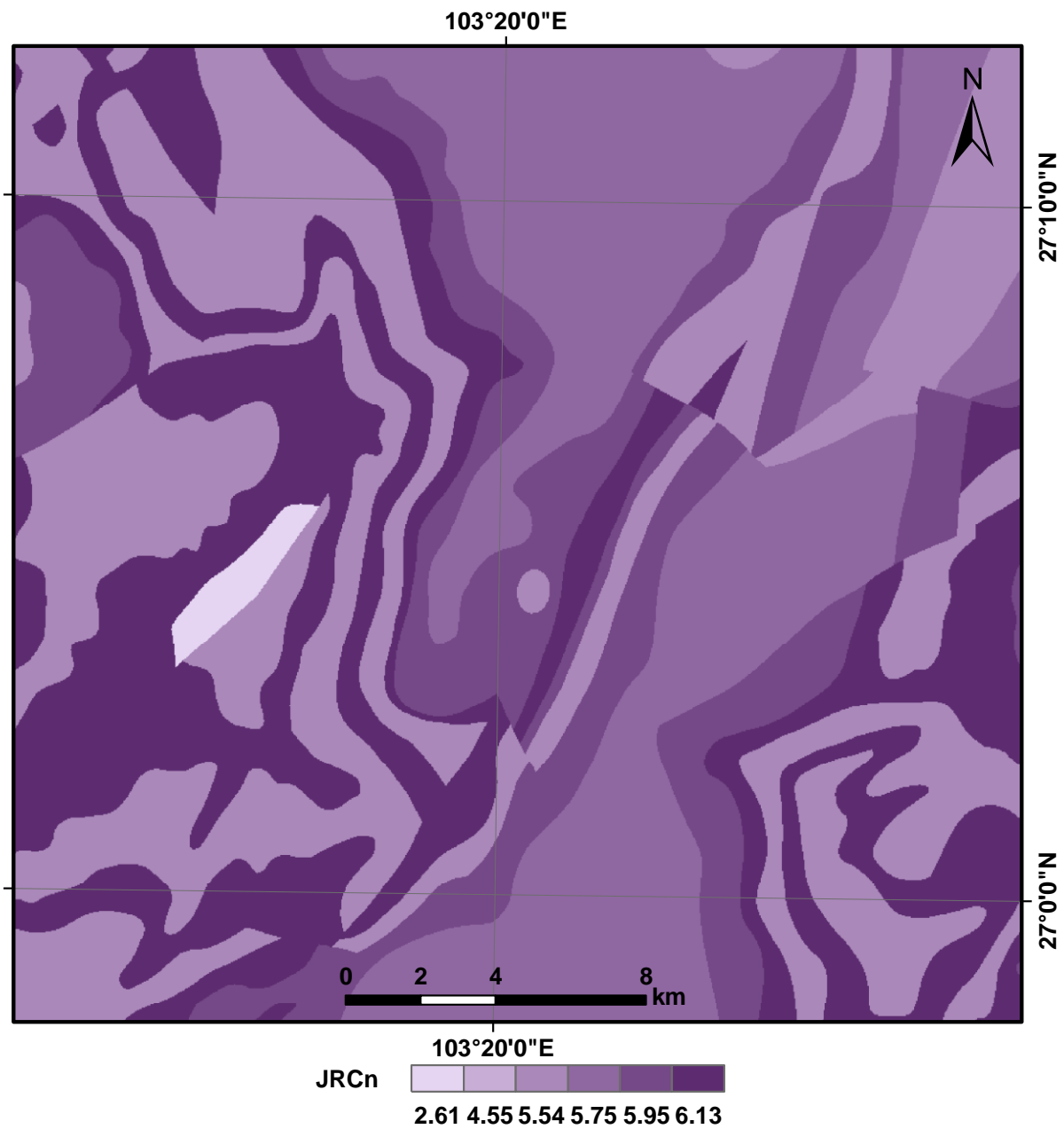
581

Fig. 8. JRC_n component of shear strength assigned to rock types in the study area.

583

Fig. 9. JCS_n component of shear strength assigned to rock types in the study area.

585
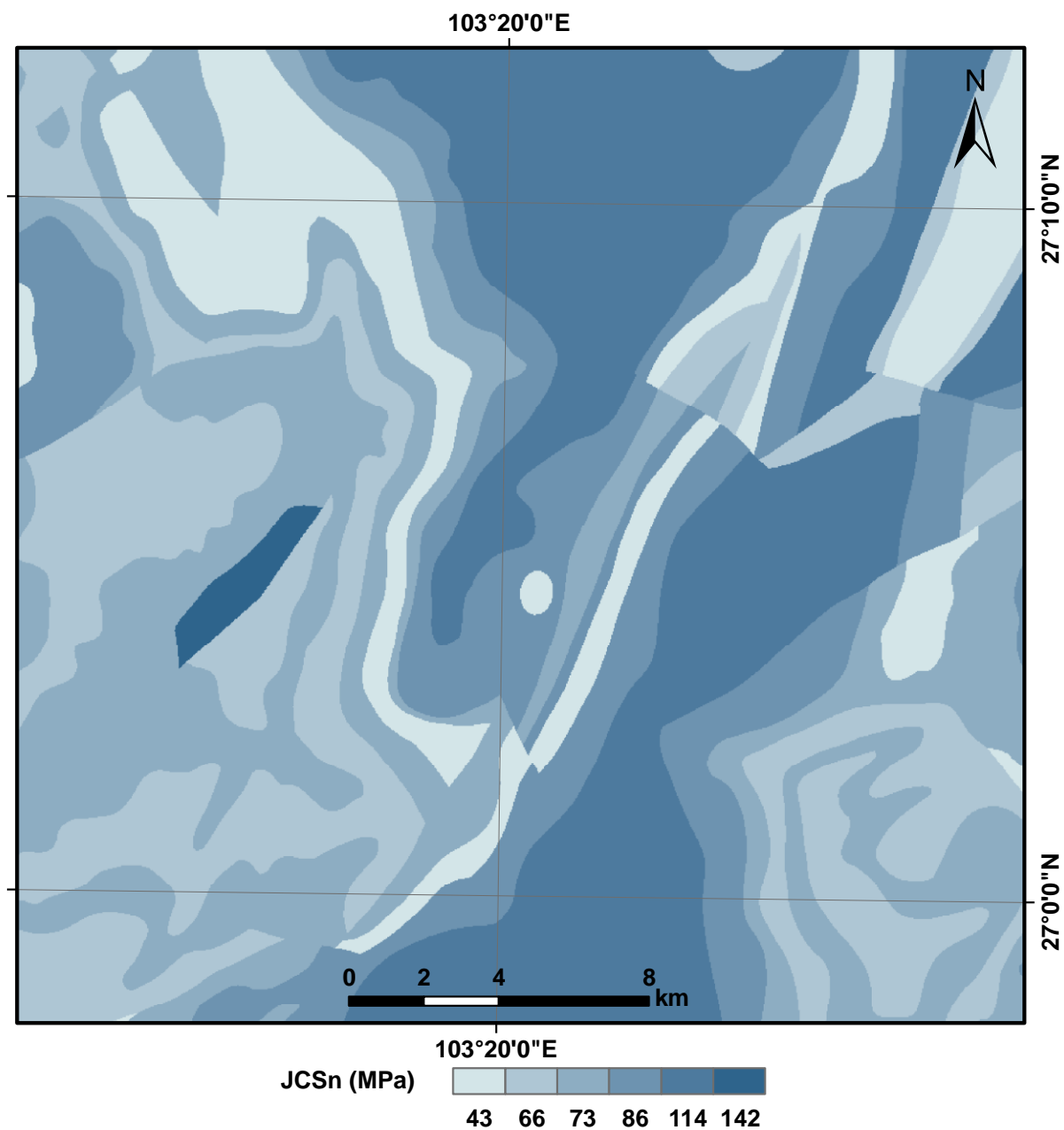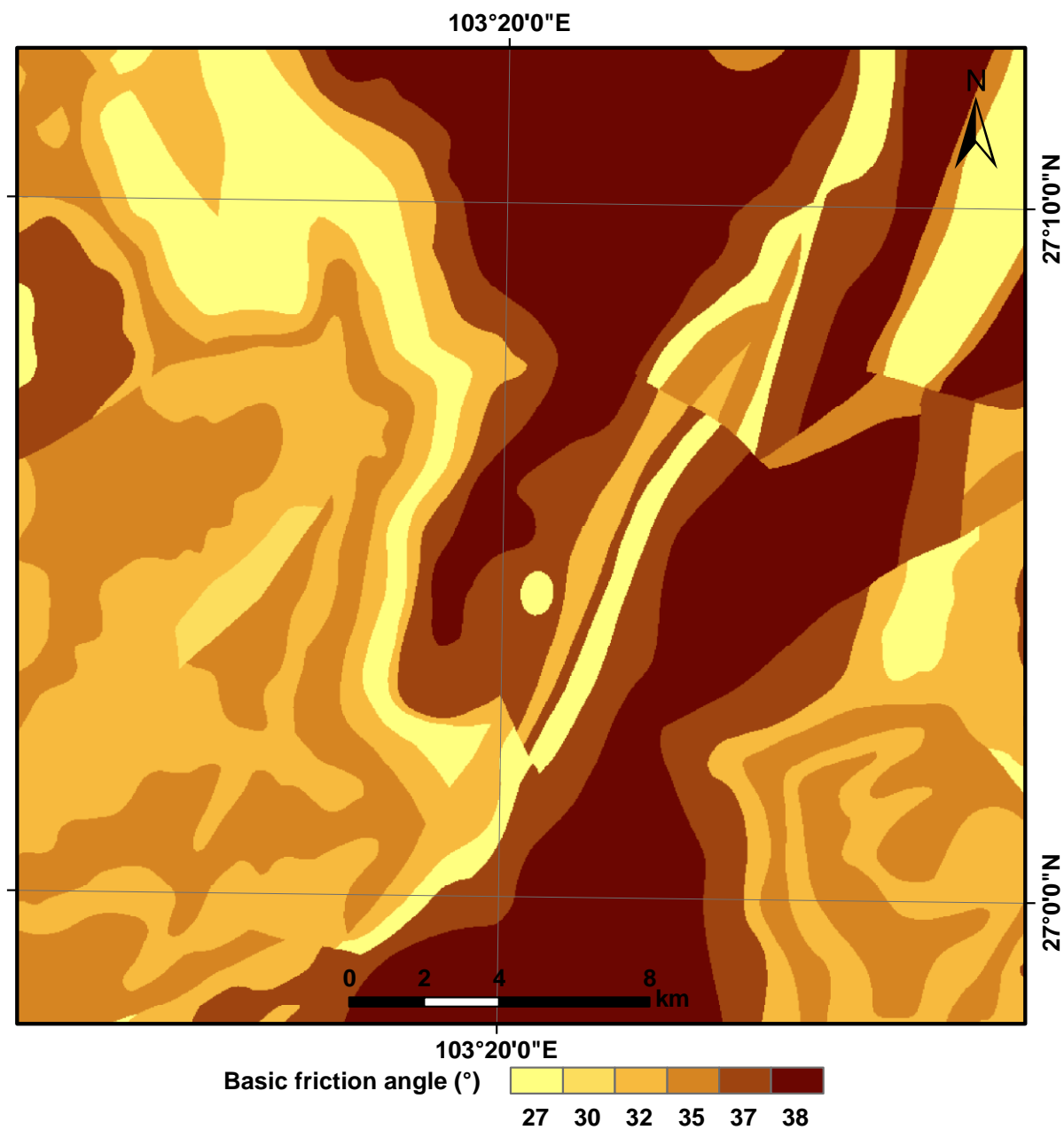
Fig. 10. Basic-friction-angle (ϕ_b) component of shear strength assigned to rock types in the study area.
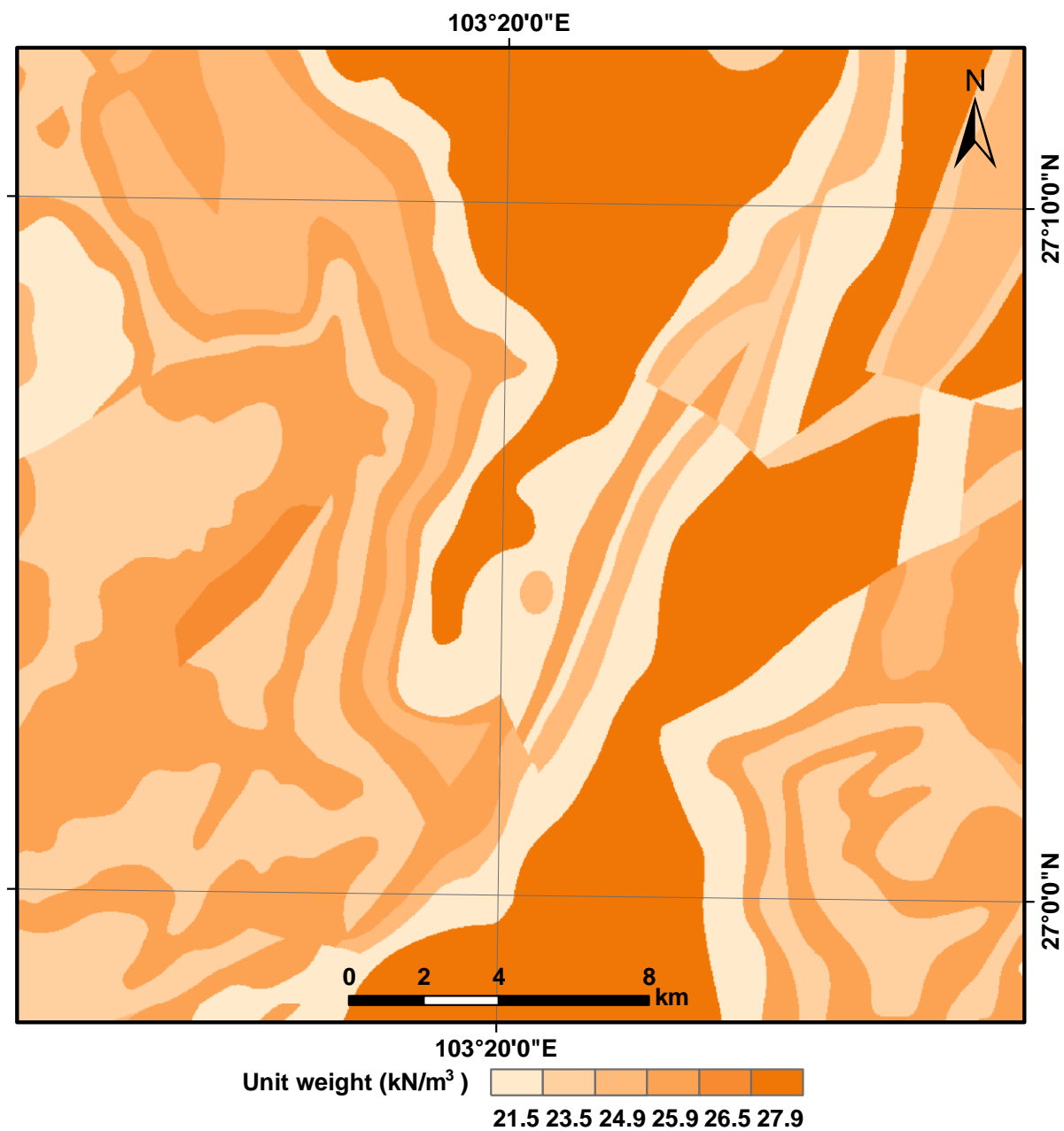
Fig. 11. Unit weight (γ) assigned to rock types in the study area.
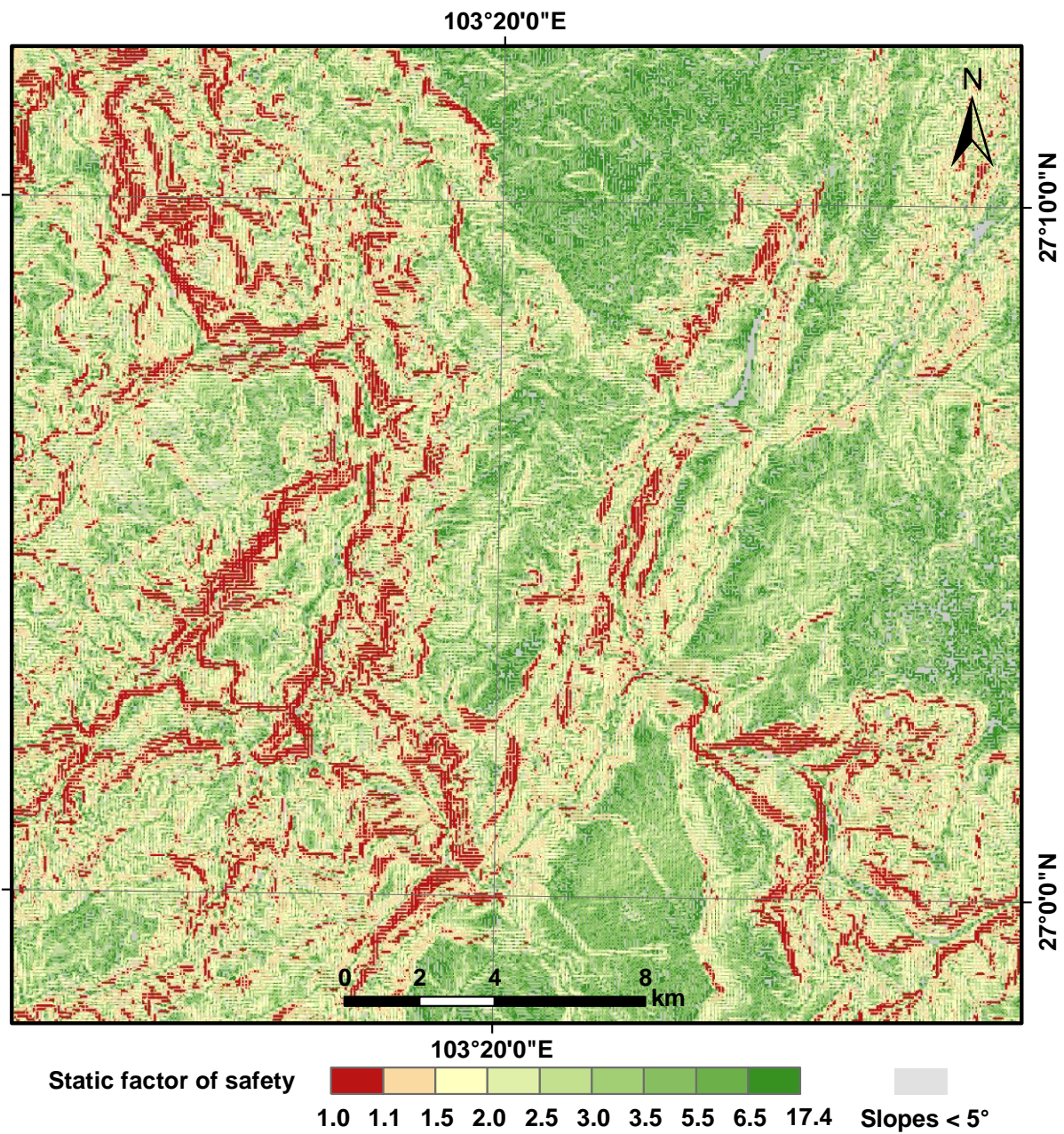
Fig. 12. Static factor-of-safety map of the study area.
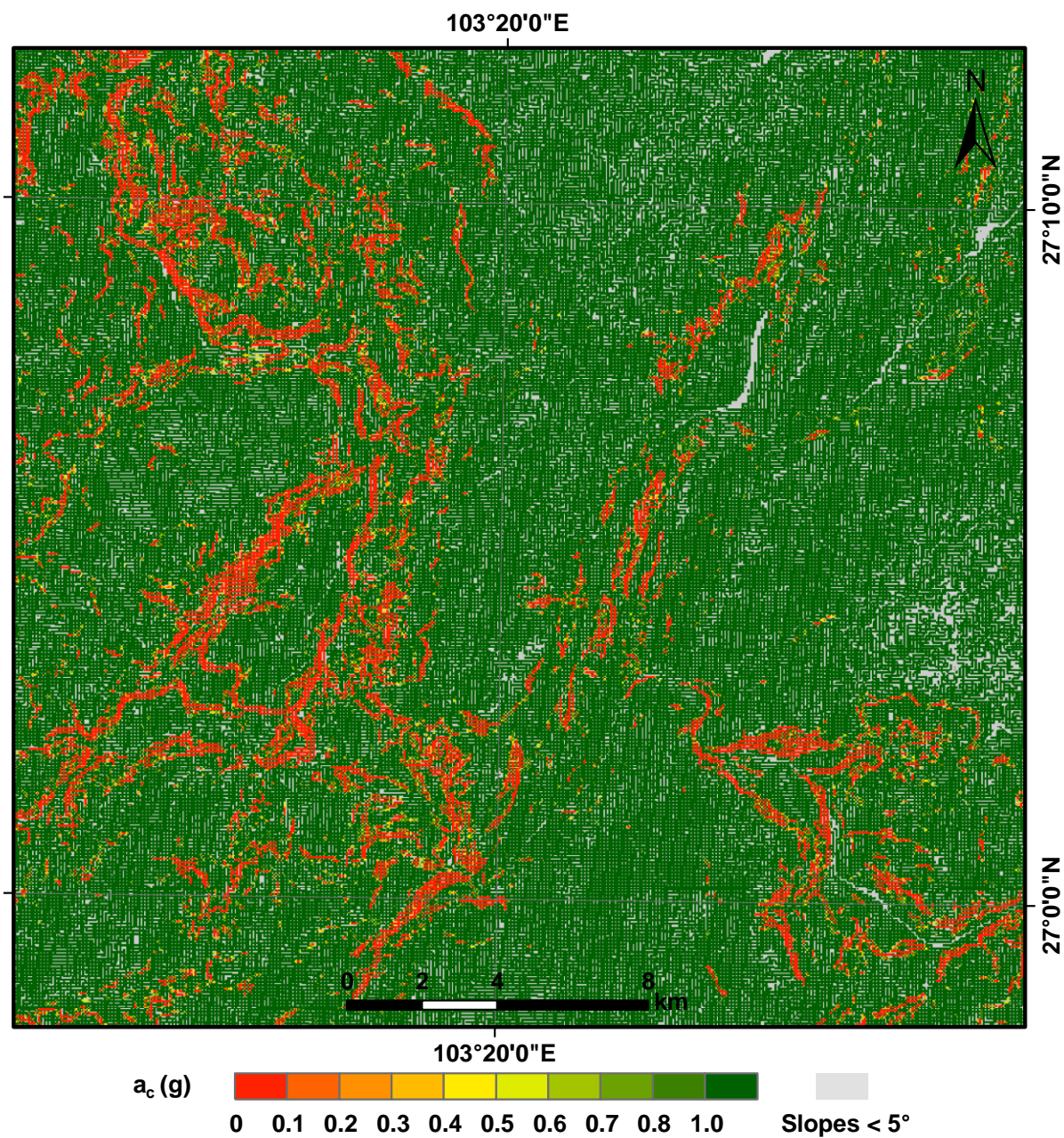
595

Fig. 13. Map showing critical accelerations in the study area.

597

598

599   **Fig. 14.** Locations of strong-motion stations.

600

601
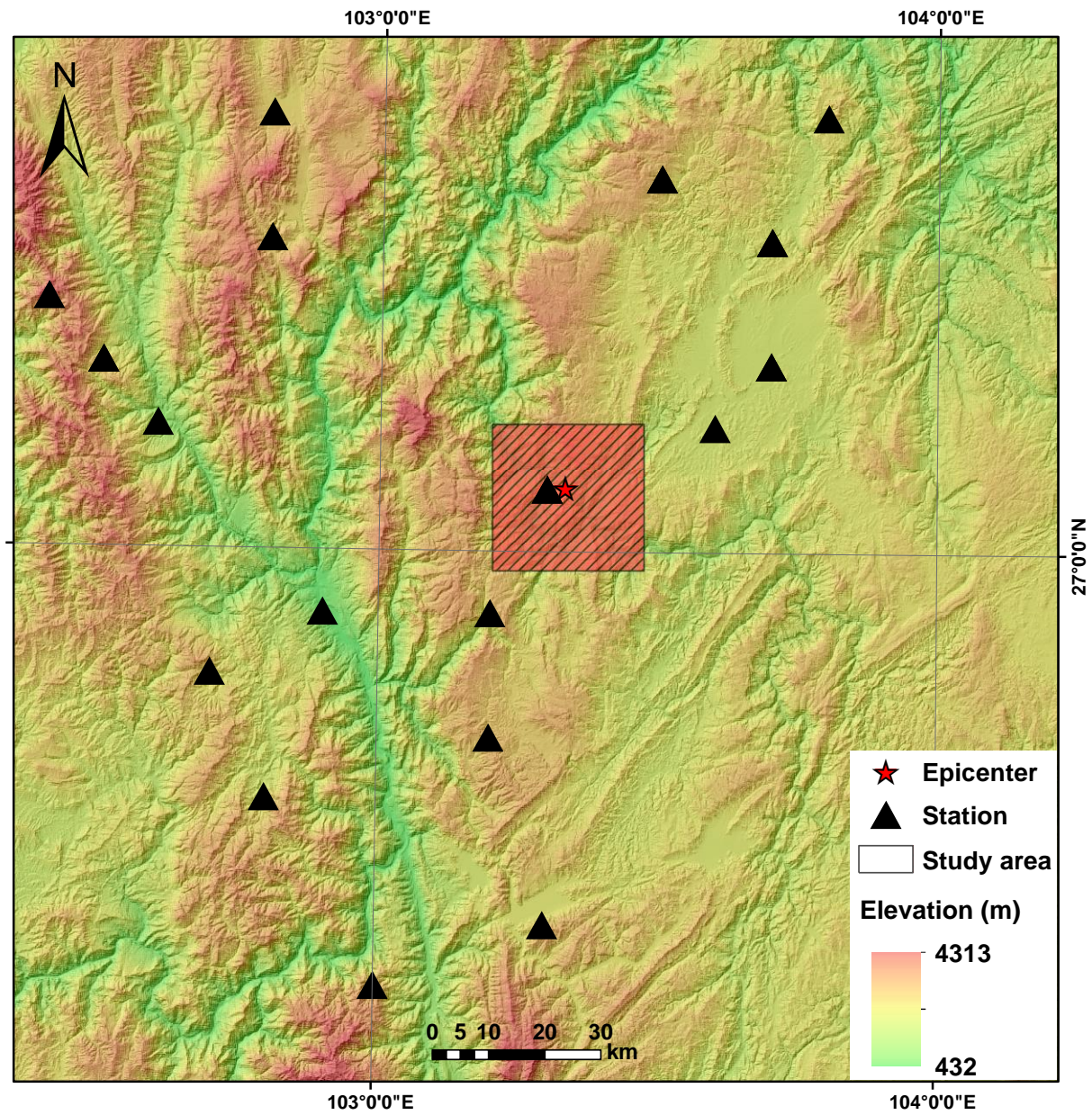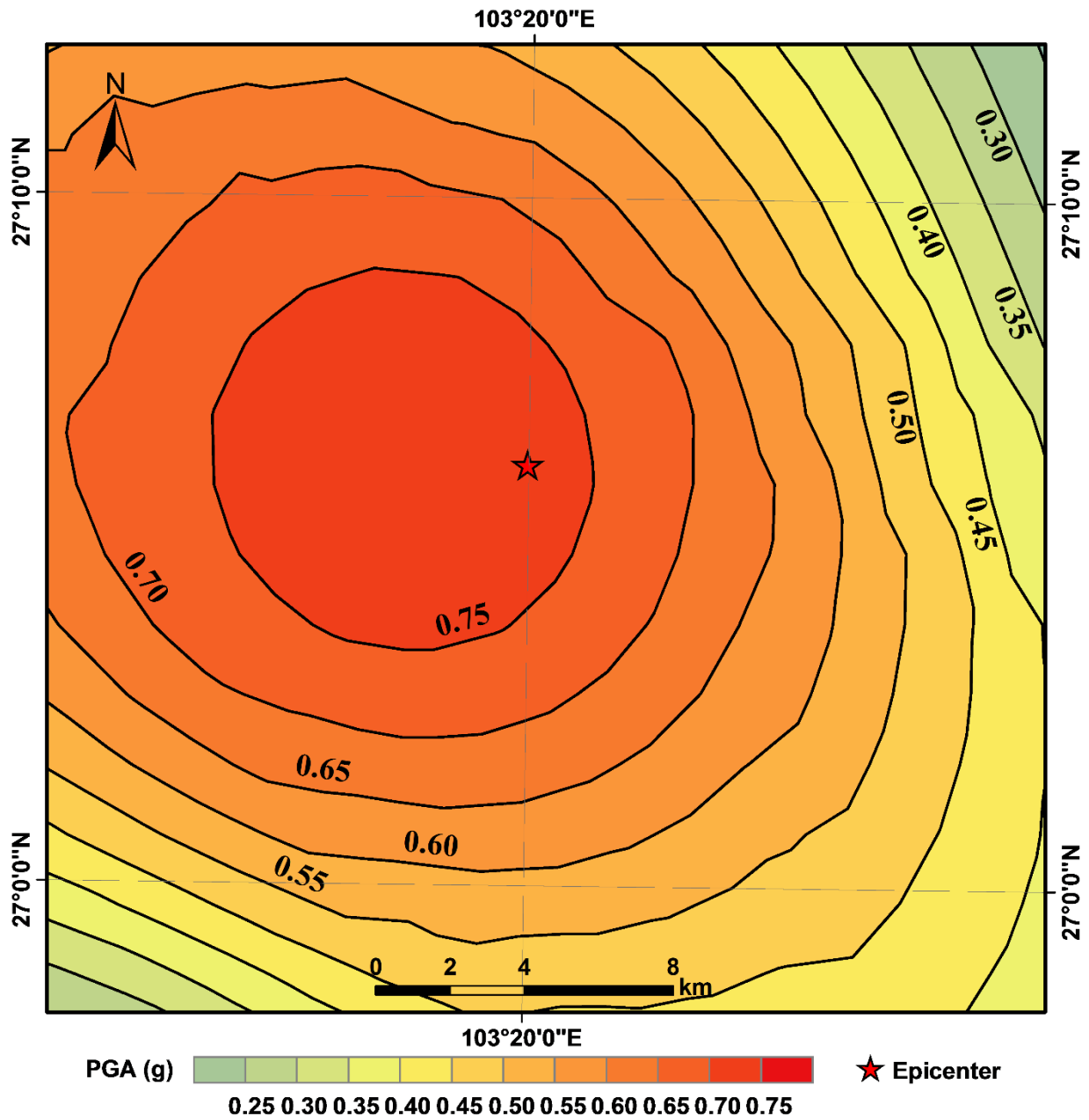
Fig. 15. Contour map of peak ground acceleration (PGA) produced by the Ludian earthquake in the

study area. PGA values shown are in g.
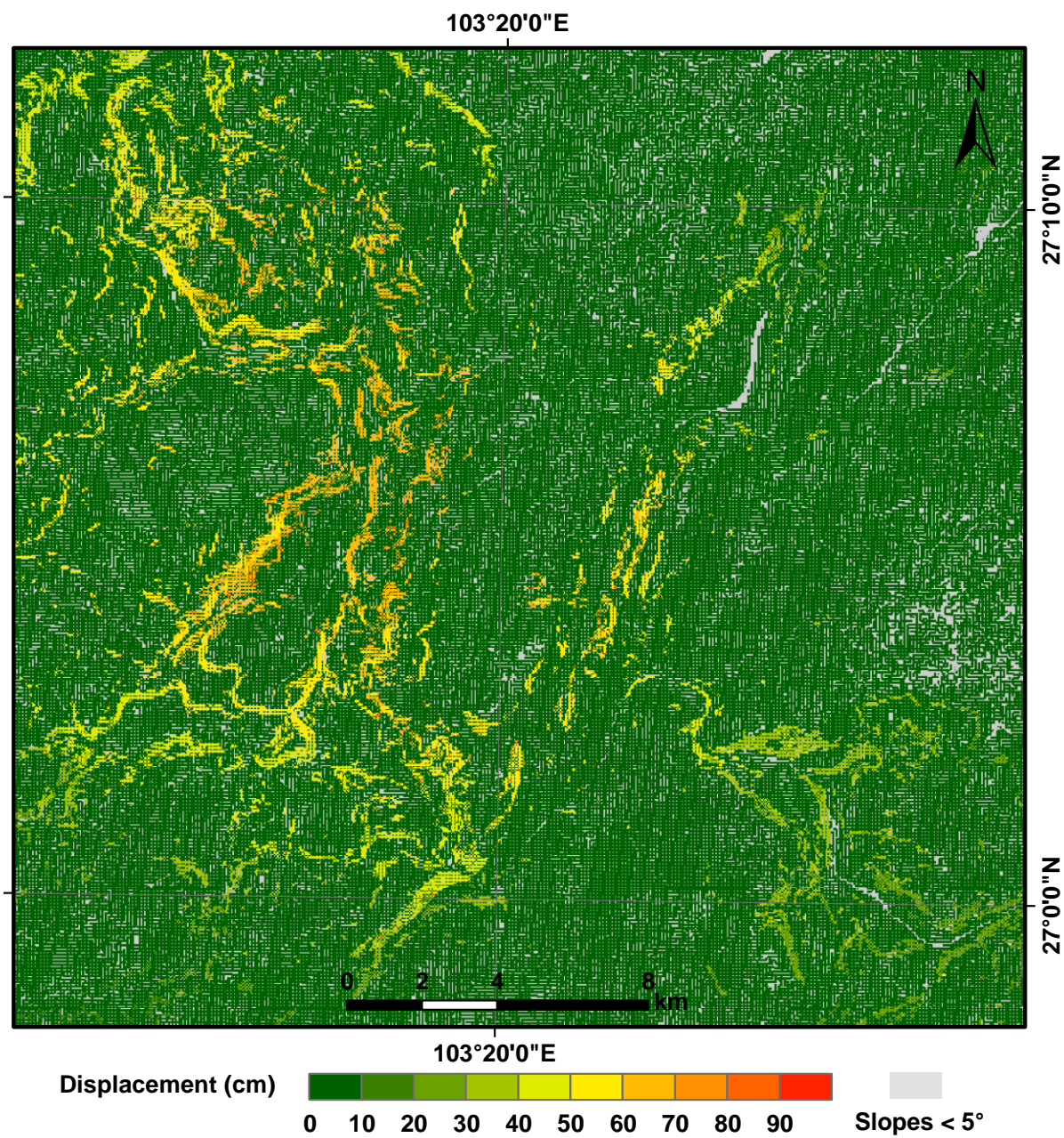
604

Fig. 16. Map showing predicted displacements in the study area.

608
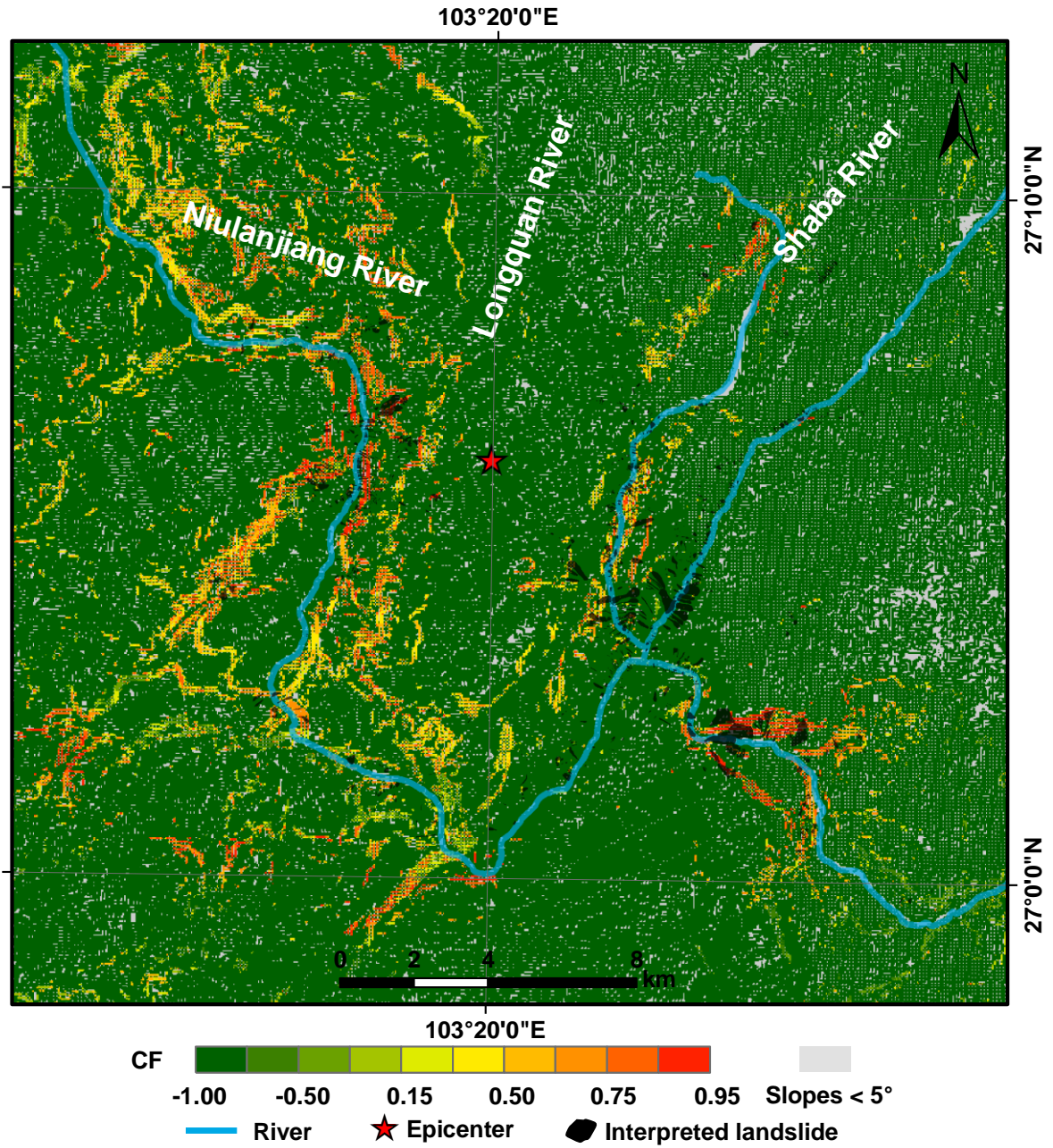
Fig. 17. Map showing confidence levels of coseismic landslides in the Ludian earthquake using the
proposed method. Confidence levels are portrayed in terms of values of *CF*.

611
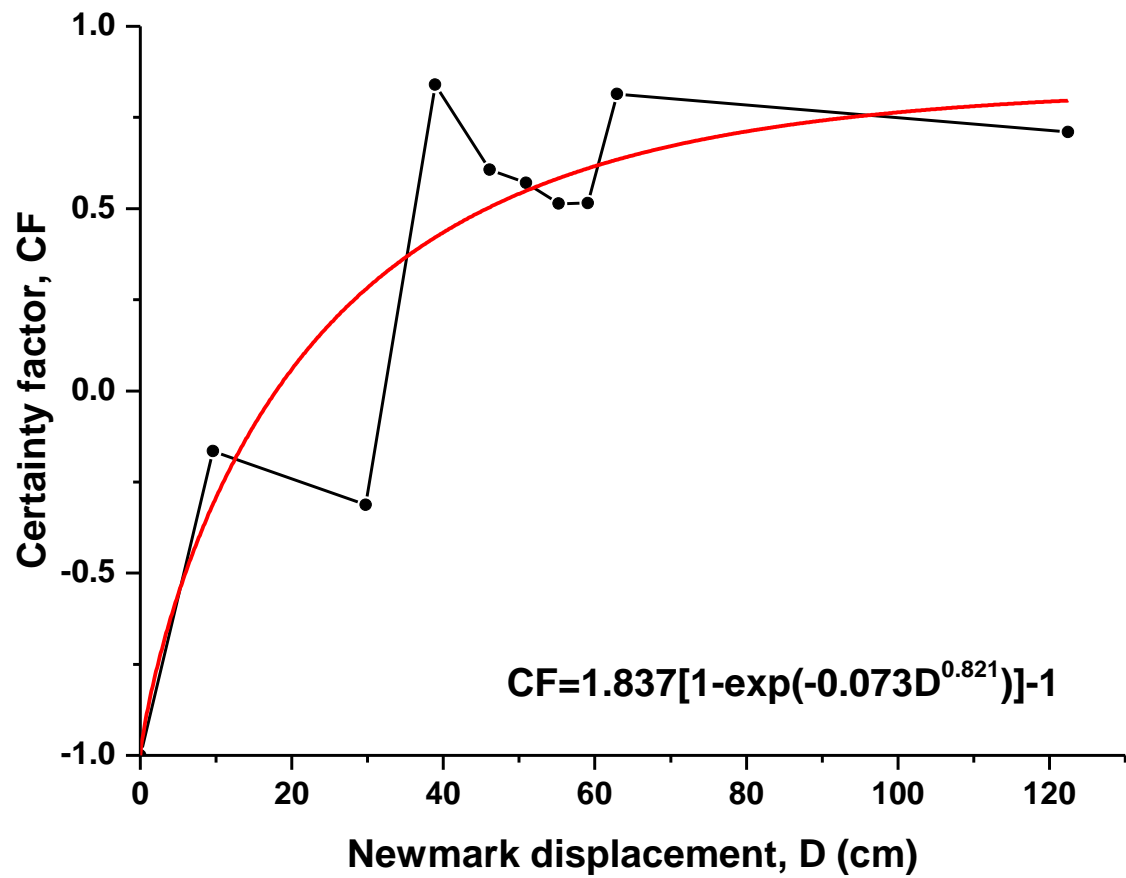
Fig. 18. Proportion of the area of landslides in each CF value area. A dot shows the CF value of

Newmark displacement bin; the red line is the fitting curve of the data using a modified Weibull function.

614

615
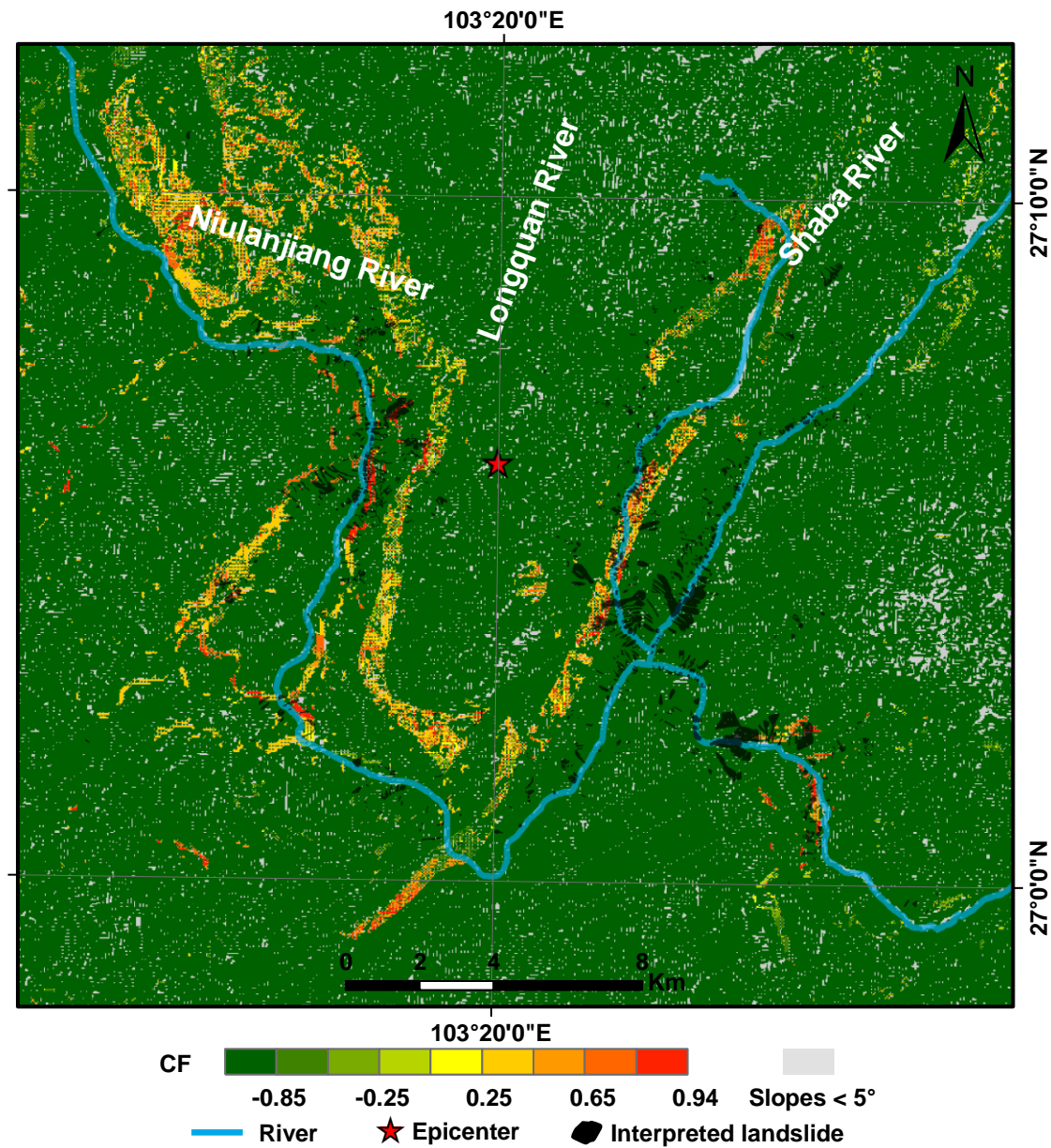
Fig. 19. Map showing confidence levels of coseismic landslides in the Ludian earthquake using a

conventional Newmark analysis. Confidence levels are portrayed in terms of values of *CF*.
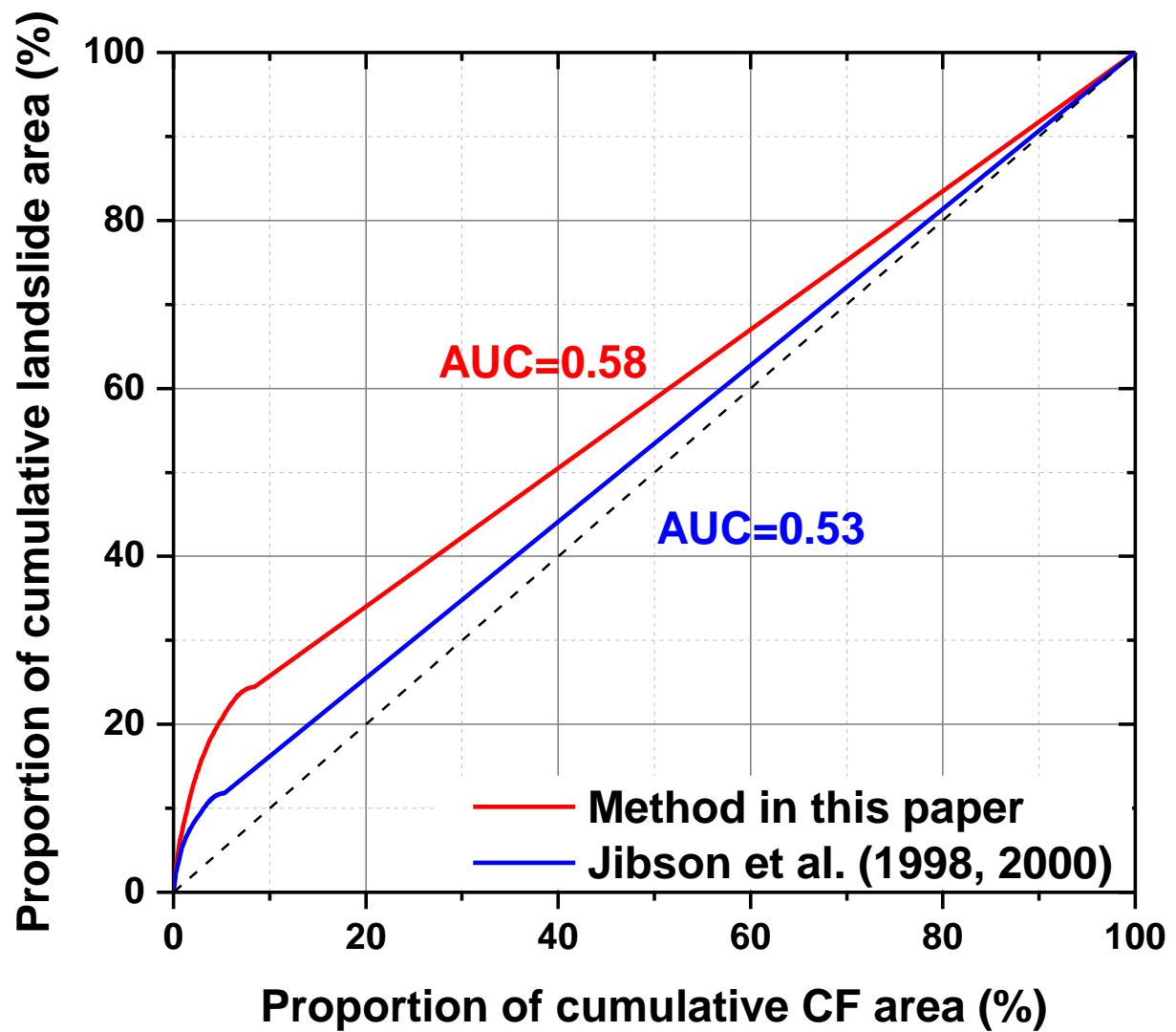
618

619

620 **Fig. 20.** Plots of area under the curve comparing the proposed method with the conventional Newmark's

621 method.

622

623 **Table Captions**

624 **Table 1.** Shear strengths assigned to rock types in the study area.

625 **Table 2.** Station records of three components of peak ground acceleration.

626

627   **Table 1**

628   Shear strengths assigned to rock types in the study area.

Rock type	γ (kN/m³)	ϕ_b	JCS_0 (MPa)	JRC_0	φ	c (kPa)	References
Dolomite	25.9	32°	140	9.5	43°	35	Singh et al., 2012 Giusepone, 2014 Alejano et al., 2014
Limestone	21.5	37°	160	9	45°	30	Bandis et al., 1983 Singh et al., 2012 Yong et al., 2018
Shale	24.9	27°	75	8	27°	16	Barton and Choubey, 1977 Bilgin and Pasamehmetoglu, 1990 Coulson, 1972
Sandstone	23.5	35°	100	6	42°	24	Bandis et al., 1983 Priest, 1993 Coulson, 1972
Basalt	27.9	38°	205	8.5	50°	40	Barton and Choubey, 1977 Alejano et al., 2014 Coulson, 1972
Slate	26.5	30°	175	3	40°	11	Barton and Choubey, 1977 Bandis et al., 1983 Alejano et al., 2012 Yong et al., 2018

629   Friction angle (φ), cohesion (c), and unit weight (γ) were derived from the Geological Engineering

630   Handbook (Geological Engineering Handbook Editorial Committee, 2018)

631

632 **Table 2**

633 Station records of three components of peak ground acceleration.

No.	Station	Epicentral distance (km)	EW (g)	NS (g)	UD (g)	Average of horizontal components (g)
1	Longtoushan 1	8.114	0.5141	0.9679	0.7193	0.7410
2	Longtoushan 2	8.3	0.9685	0.7203	0.5147	0.8444
3	Qianchang	18.6	0.1490	0.1432	0.0539	0.1461
4	Ciyuan	32.6	0.0468	0.0457	0.0265	0.0463
5	Mashu	38.5	0.1380	0.1361	0.0663	0.1370
6	Qiaojia	43	0.0253	0.0210	0.0135	0.0232
7	Zhaotong 1	47.4	0.0096	0.0152	0.0065	0.0124
8	Zhaotong 2	47.671	0.0065	0.0096	0.0088	0.0081
9	Huidongxijie	63.3	0.0123	0.0128	0.0037	0.0126
10	Maolin	64.4	0.0251	0.0184	0.0111	0.0217
11	Yongshanmaolin	65.647	0.0111	0.0252	0.0184	0.0182
12	Jingan	66.2	0.0103	0.0122	0.0062	0.0113
13	Butuotuojue	66.8	0.0118	0.0173	0.0079	0.0146
14	Zhaotongjingan	67.392	0.0062	0.0103	0.0122	0.0083
15	Huidongqianxin	67.4	0.0224	0.0223	0.0067	0.0224
16	Ningnansongxin	69.2	0.0062	0.0081	0.0032	0.0071
17	Pugebaishui	76	0.0152	0.0149	0.0066	0.0151
18	Huize	76.5	0.0164	0.0182	0.0090	0.0173
19	Pugediban	81.2	0.0186	0.0127	0.0046	0.0156
20	Butuodiban	83.7	0.0024	0.0021	0.0024	0.0023
21	Tuobuka	85.2	0.0168	0.0168	0.0136	0.0168

| 22 | Pugeyangwo | 91.4 | 0.0066 | 0.0069 | 0.0022 | 0.0068 |
| 23 | Daguan | 91.8 | 0.0043 | 0.0035 | 0.0027 | 0.0039 |

634

635